ACADÉMIE
DES SCIENCES
INSTITUT DE FRANCE

Comptes Rendus
Physique

Xiaoyong Zhang and Carlos A. R. Sá de Melo

Effects of spin–orbit coupling and Rabi fields in Tomonaga–Luttinger liquids: current status and open questions

Volume 26 (2025), p. 483-514

Online since: 15 July 2025

https://doi.org/10.5802/crphys.254

The Comptes Rendus. Physique *are a member of the Mersenne Center for open scientific publishing*
www.centre-mersenne.org — e-ISSN : 1878-1535

ACADÉMIE DES SCIENCES
INSTITUT DE FRANCE

Comptes Rendus. Physique
2025, Vol. 26, p. 483-514
https://doi.org/10.5802/crphys.254

Intervention in a conference / *Intervention en colloque*

Effects of spin–orbit coupling and Rabi fields in Tomonaga–Luttinger liquids: current status and open questions

Effets du couplage spin-orbite et des champs de Rabi dans les liquides de Tomonaga-Luttinger : état de l'art et questions ouvertes

Xiaoyong Zhang [*,a] **and Carlos A. R. Sá de Melo** [a]

[a] School of Physics, Georgia Institute of Technology, Atlanta, GA 30332, USA

E-mails: xzhang840@gatech.edu (X. Zhang), carlos.sademelo@physics.gatech.edu (C. A. R. Sá de Melo)

Abstract. We discuss the effects of spin–orbit coupling and Rabi fields in Tomonaga–Luttinger liquids for SU(2) and SU(3) Fermi systems. In the SU(2) case, we show that spin–orbit coupling and Rabi fields mix separated spin and charge excitations producing helical massless bosons, which we call Weyl bosons in analogy to their cousins, the Weyl fermions. We discuss the phase diagram and the velocities of bosonic modes, showing where different flavors of Weyl bosons emerge. We suggest that the dispersion and helicity of Weyl bosons can be detected through measurements of the the dynamical structure factor tensor. In the SU(3) case, we preliminarily discuss the effects of spin–orbit coupling and Rabi fields, and conjecture that the emergent collective modes have a scalar (charge), vector (spin) and tensor (quadrupolar) components, suggesting that these modes are more complex than Weyl bosons. To describe spin–orbit coupling, we use the terminology color-orbit coupling, where the three internal states are labeled as colors Red, Green and Blue. We discuss the phase diagram and velocities of boson modes in the non-interacting regime and ponder over several open questions that need to be addressed for SU(3) systems. Lastly, we make some concluding remarks and suggest potential experimental candidates, with two and three internal states, where spin–orbit or color-orbit coupling and Rabi fields could be used to investigate the emergence of unusual collective modes with scalar, vector and tensor properties.

Résumé. Nous étudions les effets du couplage spin-orbite et des champs de Rabi dans les liquides de Tomonaga-Luttinger pour les systèmes de fermions de symétrie SU(2) ou SU(3). Dans le cas d'une symétrie SU(2), nous montrons que le couplage spin-orbite et les champs de Rabi mélangent les excitations de spin et de charge — autrement séparées — en produisant des bosons hélicoïdaux sans masse, que nous appelons bosons de Weyl par analogie avec leurs cousins, les fermions de Weyl. Nous déterminons le diagramme de phase et les vitesses des modes bosoniques, en précisant dans quels secteurs émergent les différents types de bosons de Weyl. Nous proposons d'extraire la relation de dispersion et l'hélicité des bosons de Weyl de mesures du facteur de structure dynamique tensoriel. Dans le cas d'une symétrie SU(3), nous effectuons une première analyse des effets du couplage spin-orbite et des champs de Rabi, et conjecturons que les modes collectifs émergents ont une composante scalaire (charge), vectorielle (spin) et tensorielle (quadripolaire), ce qui suggère que ces modes sont plus complexes que les bosons de Weyl. Pour décrire le couplage spin-orbite, nous utilisons la notion de couplage couleur-orbite, où les trois états internes sont repérés par les couleurs rouge, verte et bleue. Nous discutons du diagramme de phase et des vitesses des modes de bosons

* Corresponding author

dans le régime sans interaction et réfléchissons à plusieurs questions ouvertes restant à traiter dans les systèmes de symétrie SU(3). Enfin, nous formulons quelques remarques finales et identifions des systèmes expérimentaux, à deux ou à trois états internes, dans lesquels le couplage spin-orbite ou couleur-orbite et les champs de Rabi pourraient être utilisés pour étudier l'émergence de modes collectifs inhabituels avec des propriétés scalaires, vectorielles et tensorielles.

Keywords. Spin–orbit coupling, Color-orbit coupling, Rabi fields, Tomonaga–Luttinger liquids, Weyl bosons, Interacting fermions, One dimension.

Mots-clés. Couplage spin-orbite, Couplage couleur-orbite, Champs de Rabi, Liquides de Tomonaga-Luttinger, Bosons de Weyl, Fermions en interaction, Systèmes unidimensionnels.

Manuscript received 11 January 2025, revised 2 June 2025, accepted 16 June 2025.

1. Introduction

While spin and charge are intrinsic properties of elementary particles, in one dimension (1D), interactions are responsible for the separation of spin and charge leading to spin-density (SDW) and charge-density (CDW) waves that propagate with different velocities. Spin–charge separation is theoretically described by the Tomonaga–Luttinger liquid model [1–6] in condensed matter physics (CMP), but is regarded as a general phenomenon of a large variety of quantum fields: non-Abelian Yang–Mills theory describing knotted strings as stable solitons [7–9], supersymmetric gauge theory characterizing magnetic superconductors [10], and quark-lepton unification theory suggesting the similarity between spinons and neutrinos [11]. A few experiments in condensed matter have claimed observing spin–charge separation: angle-resolved photoemission in $SrCuO_2$ [12,13] and tunneling spectroscopy in GaAs/AlGaAs heterostructures [14,15] at low temperatures. Very recently, spin–charge separation was also observed in ultracold gases (^{6}Li) as a function of interactions and temperature [16,17]. A major experimental advantage of ultracold gases over condensed matter and high energy systems is the tunability of interactions, temperature, density and external fields, permitting for a thorough exploration of spin–charge separation and mixing [16,17]. This tunability potentially allows for investigations of the interplay between spin and charge degrees of freedom in unprecedented ways like, for instance, as a function of synthetic spin–orbit coupling, Rabi (spin-flip) fields, density or chemical potential.

In CMP, spin–orbit coupling (SOC) is a relativistic quantum mechanical effect that entangles the spin of a particle to its spatial degrees of freedom. SOC plays an important role in spin-Hall systems [18,19], topological insulators [20,21] and superconductors [22–24]. However, tunability of SOC, spin-flip fields, density or chemical potential is limited. There are two common types of SOC: the Rashba [25] and the Dresselhaus [26] terms, that have been discussed in the context of semiconductors [27–32]. In ultracold atoms, SOC is synthetically created using two-photon Raman transitions instead of originating from relativistic effects [33,34]. This makes SOC tunable in bosonic [35–37] and fermionic [38–40] quantum gases, where equal mixtures of Rashba and Dresselhaus (ERD) terms have been created [35], as well as, Rashba-only (RO) [41–43]. Furthermore, Dresselhaus-only (DO) and arbitrary mixtures of Rashba and Dresselhaus terms have also been suggested [44].

In particle physics, all known elementary particles obey Pauli's spin-statistics theorem, that is, particles are either fermions with half-integer spins or bosons with integer spins [45]. The Standard Model is the theory that unifies electromagnetic, weak and strong interactions, by invoking the existence of one scalar boson (Higgs), four vector bosons (gluon, photon, Z and W), and twelve elementary fermions (six leptons and six quarks) [46,47]. All the currently known elementary fermions have spin $s = 1/2$ and can be of three types at most: Dirac, Majorana or Weyl fermions. The first type are Dirac fermions, which are massive and charged, reflecting

the existence of particles and anti-particles, like the electron and the positron [48]. The second type are Majorana fermions, which are also massive but neutral, such that the particle is also its own antiparticle [49]. The third type are Weyl fermions, which are massless Dirac fermions that become helical, as found by Weyl [50]. None of elementary Fermi particles described in the Standard Model are Weyl fermions.

In condensed matter physics, observations of Majorana fermions have been retracted [51], but there are reports that quasiparticles behave as Dirac or Weyl fermions in solid state materials. Dirac fermions emerge in cuprate superconductors [52,53], iron-based superconductors [54–56] and graphene [57]. Weyl fermions arise in the electronic structure of TaAs crystals [58,59] which do not have inversion centers and are detected as noninteracting quasiparticles via angular-resolved photoemission spectroscopy.

In solid-state condensed matter systems, one often relies on chance to discover materials with unusual properties. In ultracold atoms, however, it is common to simulate Hamiltonians found in condensed matter and particle physics, but it is also possible to design Hamiltonians possessing collective excitations or quasiparticles that go beyond those existing in standard models of condensed matter on in the Standard Model of particle physics. For example, it is possible to prepare bosonic atoms with two internal spin states creating pseudo-spin-1/2 bosons [35,37] or fermionic atoms with three internal spin states, producing pseudo-spin-1 fermions [60,61]. It is also possible to adjust the interactions of these atoms from weak (or zero) to strong using Feshbach resonances [62].

In this article, we discuss the emergence of collective modes in interacting Fermi systems that we call Weyl bosons: massless pseudospin-1/2 helical particles like Weyl fermions that arise in relativistic field theories of spin-1/2 fermions. From a more general perspective, these new types of excitations are potentially interesting, because they provide unconventional extensions of ideas that exist in the Standard Model of particle physics. In principle, Weyl bosons emerge in Fermi systems in one (1D), two (2D) and three (3D) dimensions, as a result of the existence of spin–orbit coupling, synthetic or real, and Rabi or Zeeman fields. However, we confine ourselves to the 1D case, where exact calculations can be performed in the long-wavelength-low-energy regime using the bosonization method. We discuss the creation of Weyl bosons for SU(2) (two internal states) when SOC and Rabi fields are active and conjecture the emergence of more exotic bosons, with a tensor structure, in SU(3) (three internal states) interacting Fermi systems, when color-orbit coupling and color-flip fields are present.

To explore the effects of SOC and Rabi fields on spin and charge density modes and their evolution into spin–charge-mixed helical collective modes (Weyl bosons) for SU(2) Fermi systems, as well as to investigate more exotic bosonic collective modes in SU(3) Fermi systems, we organize the remainder of this paper as follows. In Section 2, we discuss conventional spin–orbit coupling in condensed matter and synthetic spin–orbit coupling in ultracold atoms. In Section 3, we review briefly some aspects of spin–charge separation, in 1D for spin-1/2 Fermi systems, within the Tomonaga–Luttinger description, discuss bosonization in the condensed matter context, and mention some open questions that remain in this area. In Section 4, we describe SU(2) fermions with two internal states. We explore how spin and charge recombine in the presence of SOC and Rabi fields producing Weyl bosons with a maximum of two flavors, highlight experimental challenges in detecting such exotic modes in ^{6}Li, ^{40}K and ^{173}Yb via charge–charge, spin–charge and spin–spin dynamical structure factors [16,17,63,64] and discuss some open questions. In Section 5, we describe SU(3) fermions with three internal states (colors). We analyze the collective modes and their quadrupolar tensor structure in the presence of color-orbit coupling and color Rabi fields. We discuss open questions regarding the effects of SU(3) interactions, and possible experimental signatures of the emergent tensor boson modes in ^{173}Yb and ^{87}Sr. In Section 6, we present some conclusions and discuss possible theoretical and experimental outlooks.

We warn the reader that technical details, tedious derivations, and lengthy expressions are not shown in this article. We rather just outline how results are obtained and illustrate their consequences through figures. Furthermore, we set $\hbar = 1$ throughout the manuscript.

2. Synthetic spin–orbit coupling in quantum gases

Synthetic spin–orbit coupling (SOC) in quantum gases is a rapidly advancing field that merges the precise controllability of ultracold atomic systems with phenomena traditionally associated with condensed matter physics. Standard spin–orbit coupling, due to relativistic effects, plays a pivotal role in various quantum phenomena, including topological insulators, quantum spin-Hall materials, and spintronic systems [18]. In ultracold atomic gases, synthetic SOC refers to the coupling between the spin (pseudo-spin or internal state) of a particle and its center-of-mass motion, usually created via counter-propagating Raman beams. Given that SOC in cold atoms is artificially created [35,65], its highly tunable environment potentially allows for the exploration of complex quantum phases and topological states.

2.1. *Typical Hamiltonian*

For a particle of mass m and two internal states (spin 1/2), the Hamiltonian is

$$\hat{H}_1 = \frac{\hat{\mathbf{k}}^2}{2m} I + \hat{H}_{\rm SOC}, \tag{1}$$

where $\hat{\mathbf{k}}$ is the momentum operator, I is the identity matrix, and $H_{\rm SOC}$ is the spin–orbit coupling. An external potential $V_{\rm ext}(\mathbf{r})$ can also be present due to the underlying lattice structure for condensed matter systems or due to harmonic, box or optical lattice confinement for ultracold atoms. However, since we focus on the effects of spin–orbit coupling, for the reminder of our discussion, we describe only the continuum regime, where the external potential is not considered.

In the context of cold atoms, there are two types of SOC that are of general interest: the Rashba and the Dresselhaus terms. Both types of coupling were first studied in solid state materials that lack inversion symmetry and were realized synthetically in ultracold atomic systems.

In solid state materials, the Rashba SOC originates from structural inversion asymmetry, which refers to the lack of inversion symmetry due to the external constraint on the material rather than its intrinsic crystal lattice. The constraint is typically a surface or interface. At these locations, the structural asymmetry creates an effective electric field $\mathbf{E} = \mathrm{E}\mathbf{e_z}$, perpendicular to the surface/interface, which causes inversion symmetry to be broken along the z-axis (normal to the surface/interface). Due to relativistic effects, this electric field generates an effective magnetic field $\mathbf{B} = -\mathbf{k}\times\mathbf{E}/mc^2$, in SI units, at the rest frame of electrons. The $\mathbf{B}$ field couples with the spin of electrons through the Zeeman coupling $-\boldsymbol{\mu}\cdot\mathbf{B}$, where $\boldsymbol{\mu}$ is the magnetic moment, and results in the Rashba SOC Hamiltonian

$$\hat{H}_{\rm R} = \alpha_{\rm R}(\hat{\mathbf{k}}\times\mathbf{e}_z)\cdot\boldsymbol{\sigma} = \alpha_{\rm R}(\hat{k}_y\sigma_x - \hat{k}_x\sigma_y), \tag{2}$$

where $\alpha_{\rm R}$ is the Rashba coupling constant, and the electron momentum $\mathbf{k}$ in $\mathbf{B}$ is promoted to the operator $\hat{\mathbf{k}}$. As seen in Equation (2), the linear coupling between momentum and spin of electrons lifts the momentum degeneracy when $\hat{\mathbf{k}} \to -\hat{\mathbf{k}}$ in the Hamiltonian of Equation (1) using $\hat{H}_{\rm SOC} = \hat{H}_{\rm R}$.

In contrast, for solid state materials, the Dresselhaus SOC arises from bulk inversion asymmetry inherent in certain crystal lattices, particularly those lacking a center of inversion, such as zinc-blende structures (e.g., GaAs, InAs). In these materials, the SOC Hamiltonian is constrained

by the T_d (achiral tetrahedral) symmetry of the crystal, such that, close to the Γ point of the Brillouin zone, $\hat{H}_{\rm SOC}$ takes the following form

$$\hat{H}_{\rm D} = \gamma[\hat{k}_x(\hat{k}_y^2 - \hat{k}_z^2)\sigma_x + \hat{k}_y(\hat{k}_z^2 - \hat{k}_x^2)\sigma_y + \hat{k}_z(\hat{k}_x^2 - \hat{k}_y^2)\sigma_z], \tag{3}$$

where γ is the Dresselhaus coupling constant, which is determined by the material's band structure. For a two-dimensional electron gas in the xy plane, where $\langle \hat{k}_z \rangle = 0$ and $\langle \hat{k}_z^2 \rangle \neq 0$, the Dresselhaus Hamiltonian can be separated into a linear term

$$\hat{H}_{\rm D}^{(1)} = \beta_{\rm D}(\hat{k}_x\sigma_x - \hat{k}_y\sigma_y), \tag{4}$$

where $\beta_{\rm D} = -\gamma\langle \hat{k}_z^2 \rangle$ is the effective Dresselhaus coupling constant, and a cubic term

$$\hat{H}_{\rm D}^{(3)} = \gamma(\hat{k}_x\hat{k}_y^2\sigma_x - \hat{k}_y\hat{k}_x^2\sigma_y). \tag{5}$$

In the low-momentum regime, only the linear term is generally considered, because it is typically orders of magnitude larger than the cubic term. In the remainder of this article, the linear Dresselhaus Hamiltonian $\hat{H}_{\rm D}^{(1)}$ is referred to as $\hat{H}_{\rm D}$ without the cubic contribution.

A more general case in solid state materials includes both Rashba and Dresselhaus SOC leading to

$$\hat{H}_{\rm SOC} = \alpha_{\rm R}(\sigma_x\hat{k}_y - \sigma_y\hat{k}_x) + \beta_{\rm D}(\hat{k}_x\sigma_x - \hat{k}_y\sigma_y). \tag{6}$$

The special case of equal Rashba and Dresselhaus (ERD) SOC, that is, $\alpha_{\rm R} = \beta_{\rm D} = \alpha$, leads to

$$\hat{H}_{\rm ERD} = \alpha(\hat{k}_x + \hat{k}_y)(\sigma_x - \sigma_y). \tag{7}$$

A global unitary SU(2) rotation $U = I/\sqrt{2} + {\rm i}(\sigma_x + \sigma_y)/2$, where I is the identity matrix, brings the Hamiltonian to $\hat{H}_{\rm ERD} = -2\alpha\hat{k}_+\sigma_z$, where $\hat{k}_+ = (\hat{k}_x + \hat{k}_y)/\sqrt{2}$. In 1D systems, $\hat{k}_+ = \hat{k}_x/\sqrt{2}$, giving

$$\hat{H}_{\rm ERD} = -\sqrt{2}\alpha\hat{k}_x\sigma_z. \tag{8}$$

The ERD Hamiltonian has been synthesized in ultracold atomic systems [35,65], and are briefly reviewed next.

2.2. *Synthetic SOC via Raman coupling*

Using pairs of Raman beams, spin–orbit coupling has been realized in ^{87}Rb Bose–Einstein condensates [35], as well as, in fermionic systems like ^{6}Li [38] and ^{40}K [66]. Heating effects can be substantial in ^{6}Li, but may be manageable in ^{40}K. While most experiments utilize two internal states of the atoms to create an SU(2) SOC, it is also possible to create SOC for atoms with N internal states and SU(N) symmetric interactions like in ^{173}Yb [67,68] and ^{87}Sr [69]. Next, we discuss the experimental realization of SOC in ultracold atoms with two or three internal states, which is relevant for the posterior discussion of systems with SU(2) and SU(3) invariant interactions.

We consider a cloud of ultracold atoms with two internal states labeled as $|\uparrow\rangle$, $|\downarrow\rangle$ and a higher energy excited state $|e\rangle$. Two laser beams with frequencies ω_1, ω_2 and wavevectors $\mathbf{k}_1$, $\mathbf{k}_2$ can couple to the atoms, driving Raman transitions between the pseudo-spin-1/2 states via the excited state $|e\rangle$, as shown in Figure 1(a). The Hamiltonian describing the Raman coupling is

$$\hat{H}_{\rm RC} = -\tfrac{1}{2}[\Omega_1 {\rm e}^{{\rm i}(\mathbf{k}_1\cdot\mathbf{r}-\omega_1 t)}|e\rangle\langle\uparrow| + \Omega_2 {\rm e}^{{\rm i}(\mathbf{k}_2\cdot\mathbf{r}-\omega_2 t)}|e\rangle\langle\downarrow| + {\rm H.c.}], \tag{9}$$

where use the convention $|\uparrow\rangle$ is state $|1\rangle$ (low energy), and $|\downarrow\rangle$ is state $|2\rangle$ (high energy) for the matrix notation of $\hat{H}_{\rm RC}$. Here, Ω_1 and Ω_2 are the Rabi frequencies, taken to be real, $\mathbf{r}$ is the position of the atom, and H.c. denotes Hermitian conjugation. In the experimental setup, the one-photon detuning $|\Delta|$ (the difference between the laser frequencies and the excited state's energy) is large

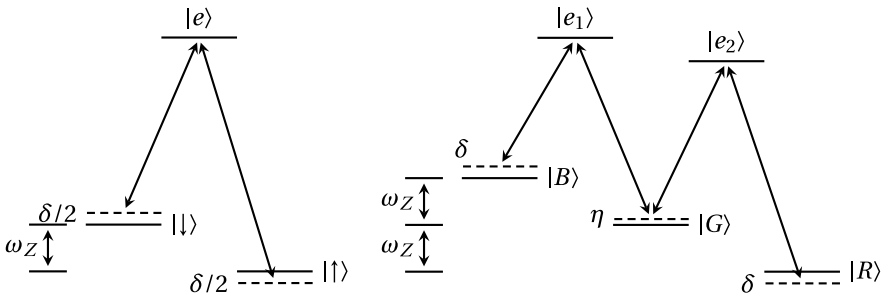

(a) Two levels **(b)** Three levels

Figure 1. Energy level diagrams showing the Raman processes used to synthesize spin–orbit coupling for (a) two-level ($|\uparrow\rangle, |\downarrow\rangle$) and (b) three-level ($|R\rangle, |G\rangle, |B\rangle$) systems. The frequencies ω_Z are Zeeman shifts, δ is the detuning and η is a reference energy, while $|e\rangle, |e_1\rangle$ and $|e_2\rangle$ are intermediate higher-energy states used by the Raman beams.

compared to $|\Omega_1|$ and $|\Omega_2|$, allowing for the the excited state $|e\rangle$ to be adiabatically eliminated [70]. Then, the effective Hamiltonian in the rotating-frame becomes

$$\hat{H}_{\rm RC}^{\rm eff} = \frac{1}{2}\begin{pmatrix} -\delta & \Omega e^{-i2\mathbf{k}_T\cdot\mathbf{r}} \\ \Omega e^{i2\mathbf{k}_T\cdot\mathbf{r}} & \delta \end{pmatrix}, \tag{10}$$

where $\Omega = \Omega_1\Omega_2/2\Delta$ is the effective two-photon Rabi frequency, $\mathbf{k}_T = (\mathbf{k}_1 - \mathbf{k}_2)/2$ is a measure of the momentum transferred to the atoms, $\delta = \omega_Z - \omega$ is the detuning from the Raman transition, ω_Z is the splitting between the two internal states and $\omega = \omega_1 - \omega_2$ is the two-photon detuning.

Using the kinetic energy operator $\hat{H}_{\rm K} = (\hat{\mathbf{k}}^2/2m)I$, where I is the identity matrix, and performing a suitable global SU(2) transformation, leads to the standard Hamiltonian matrix with kinetic, SOC and Rabi/Zeeman terms [35]

$$\hat{H}_{\rm KS} = \frac{(\hat{\mathbf{k}}I - \mathbf{k}_T\sigma_z)^2}{2m} - \frac{\delta}{2}\sigma_z + \frac{\Omega}{2}\sigma_x = \left(\frac{\hat{\mathbf{k}}^2 + \mathbf{k}_T^2}{2m}\right)I - \left(\frac{\mathbf{k}_T}{m}\right)\cdot\hat{\mathbf{k}}\sigma_z - \frac{\delta}{2}\sigma_z + \frac{\Omega}{2}\sigma_x, \tag{11}$$

where $\mathbf{k}_T$ and $-\mathbf{k}_T$ are the momentum transferred to the $|\uparrow\rangle$ and $|\downarrow\rangle$, respectively, and $\{\sigma_x, \sigma_y, \sigma_z\}$ are the Pauli matrices. The second term in Equation (11) explicitly shows the coupling between the momentum operator $\hat{\mathbf{k}}$ and spin matrix σ_z, which corresponds to the ERD SOC introduced in Section 2.1.

Spin–orbit coupling for three internal states can also be created experimentally using a pair of counter-propagating Raman beams, as in ^{87}Rb at the $F = 1$ manifold of a Bose–Einstein condensate (BEC) [71]. A pair of counterpropagating Raman beams along the x-axis with frequencies ω_L and $\omega_L + \delta\omega_L$ are used to create the SOC. These beams couple atomic states $|m_{\rm F}, k_x\rangle$ that differ by one unit of internal angular momentum ($\hbar = 1$). The Zeeman field B_0 is applied along the y-direction to produce the Zeeman shift $\omega_Z = g\mu_B B_0 \approx \delta\omega_L$. Then, the Hamiltonian matrix with kinetic, SOC and Rabi/Zeeman terms is [60,61,70,71]

$$\hat{H}_{\rm KS} = \begin{pmatrix} \frac{(\hat{k}_x - k_T)^2}{2m} + \frac{\hat{\mathbf{k}}_\perp^2}{2m} - \delta & \frac{\Omega_{\rm R}}{2} & 0 \\ \frac{\Omega_{\rm R}}{2} & \frac{\hat{k}_x^2}{2m} + \frac{\hat{\mathbf{k}}_\perp^2}{2m} + \eta & \frac{\Omega_{\rm R}}{2} \\ 0 & \frac{\Omega_{\rm R}}{2} & \frac{(\hat{k}_x + k_T)^2}{2m} + \frac{\hat{\mathbf{k}}_\perp^2}{2m} + \delta \end{pmatrix}, \tag{12}$$

where $\hat{\mathbf{k}}_\perp = (\hat{k}_y, \hat{k}_z)$ is the transverse momentum (yz plane) of the atom, $\Omega_{\rm R}$ is the resonant Rabi frequency, $\delta = \omega_Z - \delta\omega_L$ is the detuning from the Raman resonance, and η is a quadratic Zeeman shift, and $k_T = 2k_{\rm R}$, where $k_{\rm R}$ is the wavenumber (momentum) of each Raman beam, is the

magnitude of the momentum transferred to the lowest and highest energy state. In Figure 1(b), we show the corresponding level diagram.

A similar three-internal-state Hamiltonian with SOC and Rabi fields was used to investigate Fermi liquid properties for pseudo-spin-1 fermions [60] and exotic topological color superfluidity for fermions with SU(3) attractive interactions [61] in three dimensions. However, in this manuscript, we concentrate on the effects of SOC in one dimensional systems for two reasons. First, because we are interested in the emergence of bosonic helical modes (Weyl bosons) for SU(2) Fermi systems with two internal states, where spin and charge are initially separated, and analytical results can be obtained via bosonization. Second, because we are fascinated by the potential realization of tensor bosons for SU(3) Fermi systems with three internal states, where exact results may also obtained, via the bosonization technique, in the low-frequency and long-wavelength regimes. For pedagogical reasons, we discuss first the interacting Fermi gas with two internal spin states in 1D, without SOC and Rabi fields, to introduce the bosonization technique that is later applied to the same system in the presence of SOC and Rabi fields.

3. Spin–charge separation in 1D interacting fermions

In conventional higher-dimensional (2D and 3D) systems, electrons are elementary particles that carry both spin and charge densities that propagate with the same velocity. However, in 1D systems, electron–electron interactions may lead to the decoupling of spin and charge degrees of freedom under certain conditions. This decoupling results in the emergence of separate collective excitations describing charge density and spin density waves that propagate at different velocities. The physics of interacting 1D Fermi gases was explored early on by Tomonaga and Luttinger [1,2], and later developed into the Tomonaga–Luttinger liquid theory, via the development of bosonization techniques [3,72], which became a powerful tool for the discovery of spin–charge separation in 1D Fermi systems. There have been claims of experimental observations of spin–charge separation in semiconductor nanowires and quasi-1D organic conductors [12,73]. More recently, claims of spin–charge separation have also been made in 1D ultracold atomic gases [16]. In this section, we review the basics of the bosonization method, that leads to spin–charge separation in 1D continuum Fermi gases with sufficiently long-ranged interactions.

3.1. *Bosonization and spin–charge separation*

For a comprehensive introduction to bosonization and spin–charge separation in 1D systems, we refer the reader to standard textbooks [4,5]. Consider a 1D Fermi gas with mass m, two spin states and kinetic energy operator

$$\hat{H}_{\rm kin} = \sum_{ks} \frac{k^2}{2m} c_s^\dagger(k) c_s(k), \tag{13}$$

where k is the one-dimensional momentum and s is the spin label. The Fermi surface for a degenerate gas of fermions in 1D consists of points. For sufficient low energies, we linearize the kinetic energy operator around the Fermi points ($\pm k_{\rm F}$) leading to

$$\hat{H}_{\rm kin} = \sum_{ksr} \{E_{\rm F} + {\rm sgn}(r)\, v_{\rm F}[k - {\rm sgn}(r)\, k_{\rm F}]\} c_{sr}^\dagger(k) c_{sr}(k), \tag{14}$$

where $r = \{L, R\}$ represents the linearized band on the left near $-k_{\rm F}$ or on the right near $+k_{\rm F}$, $E_{\rm F} = k_{\rm F}^2/2m$ is the Fermi energy, and $v_{\rm F} = k_{\rm F}/m$ is the Fermi velocity. The function ${\rm sgn}(r)$ gives the sign of the slope and of the corresponding Fermi momentum: ${\rm sgn}(L) = -1$, ${\rm sgn}(R) = +1$. The reference Hamiltonian $\hat{H}_0 = \sum_{ksr} E_{\rm F} c_{sr}^\dagger(k) c_{sr}(k)$, corresponding to the energy $E_0 = N E_{\rm F}$, where N is the total number of fermions, is set to zero without loss of generality. Thus, we drop this reference term from the kinetic energy operator $\hat{H}_{\rm kin}$ from now on.

A typical interaction between the fermions can be modeled as

$$\hat{H}_{\rm int} = \frac{1}{2L_b} \sum_{kk'qss'} V_{ss'}(q) c_s^\dagger(k-q) c_{s'}^\dagger(k'+q) c_{s'}(k') c_s(k), \tag{15}$$

where $V_{ss'}(q)$ is the interaction with real (momentum) space range R_0 ($q_0 = 2\pi/R_0$) and dimensions of energy times length, and L_b is the length of the system. The interaction may have different origins depending on the physics manifested in the system: for example, it can be Coulomb interactions, involving direct and exchange contributions for charged fermions, effective interactions with finite range for charged or neutral fermions, or SU(2) invariant interactions for neutral fermions. In the analysis below the interactions are not too strong, that is, $|V_{s,s'}(q)|/L_b \ll NE_{\rm F}$ for all q. Furthermore, when the range R_0 is sufficiently large, only small momentum transfers q contribute significantly to the interaction Hamiltonian, that is, the terms with $qR_0 \ll 1$ are dominant. Furthermore,large momentum transfers are found to be irrelevant in renormalization group approaches [4,5,74]. Thus, for spin-independent interactions $V_{ss'}(q) = V(q)$, the interaction Hamiltonian acquires, in the long wavelength limits ($q \approx 0$), a density–density form [4,5]

$$\hat{H}_{\rm int} = \frac{1}{2L_b} \sum_{qss'r} \left[g_4 \hat{\rho}_{sr}(q) \hat{\rho}_{s'r}(-q) + g_2 \hat{\rho}_{sr}(q) \hat{\rho}_{s'\bar{r}}(-q) \right], \tag{16}$$

where $\hat{\rho}_{sr}(q) = \sum_k c_{sr}^\dagger(k) c_{sr}(k+q)$ is the Fourier transform of the real-space spin-dependent density operator in branch r. For spin-dependent interactions $V_{ss'}(q)$, the terms $g_2 \to g_{2ss'}(q)$ and $g_4 \to g_{4ss'}(q)$ carry s and s' subscripts and are proportional to $V_{ss'}(q)/2$. Here, g_2 and g_4 have dimensions of energy times length. In Equation (16), the term with coefficient g_4 couples fermions on the same side of the Fermi surface, while the term with coefficient g_2 couples fermions from one side of the Fermi surface with fermions on the other side. Both g_2 and g_4 are small-momentum-transfer ($q \approx 0$) scattering processes. We do not consider large-momentum-transfer ($q \approx 2k_{\rm F}$) terms, called g_1, because the finite-ranged interaction produces $g_1 \ll \min\{g_2, g_4\}$, which also becomes irrelevant from the renormalization group point of view [4,5,74]. In passing, we note that for the Coulomb interaction $g_2 = g_4$ and both terms depend logarithmically in $|q|$ [75], however for a more generic effective finite-ranged interactions $g_2 \to g_2(q \approx 0)$ and $g_4 \to g_4(q \approx 0)$, g_2 also may be different from g_4, a condition used in the discussion below.

To obtain the spin and charge modes, we use the bosonization technique. Boson operators are constructed as [4,5]

$$b_s^\dagger(q) = \sqrt{\frac{2\pi}{|q|L_b}} \Theta(-{\rm sgn}(r)q) \hat{\rho}_{sr}(q), \tag{17}$$

satisfying standard bosonic commutation relations. Here, $\Theta(x)$ is the Heaviside step function. Using these boson operators and defining the momentum $q = k - {\rm sgn}(r)k_{\rm F}$, the kinetic part of the Hamiltonian becomes

$$\hat{H}'_{\rm kin} = \sum_{qs} v_{\rm F}|q| b_s^\dagger(q) b_s(q). \tag{18}$$

This is not exactly the original kinetic energy operator, but is a valid representation of it in the low-momentum limit, due to the commutation relation

$$[\hat{H}_{\rm kin}, b_s(q)] = [\hat{H}'_{\rm kin}, b_s(q)] = -v_{\rm F}|q| b_s(q), \tag{19}$$

that secures the equivalency between $\hat{H}_{\rm kin}$ in the fermionic representation and $\hat{H}'_{\rm kin}$ in the bosonic one. Thus, we use the equivalence between $\hat{H}'_{\rm kin}$ and $\hat{H}_{\rm kin}$, to write the full Hamiltonian $\hat{H} = \hat{H}_{\rm kin} + \hat{H}_{\rm int}$ as a quadratic form of the bosonic operators:

$$\hat{H} = \sum_q \left\{ v_{\rm F}|q| \sum_s b_s^\dagger(q) b_s(q) + |q| \sum_{ss'} \left[\frac{g_4}{4\pi} b_s^\dagger(q) b_{s'}(q) + \frac{g_2}{4\pi} b_s^\dagger(q) b_{s'}^\dagger(-q) + {\rm H.c.} \right] \right\}. \tag{20}$$

Next, we define boson operators in the charge and spin sectors

$$b_\rho^\dagger(q) = \frac{1}{\sqrt{2}}(b_\uparrow^\dagger(q) + b_\downarrow^\dagger(q)) \quad \text{and} \quad b_\sigma^\dagger(q) = \frac{1}{\sqrt{2}}(b_\uparrow^\dagger(q) - b_\downarrow^\dagger(q)), \tag{21}$$

where $b_\rho^\dagger(q)$ creates an excitation in the charge density sector and $b_\sigma^\dagger(q)$ creates an excitation in the spin density sector. In this basis, the Hamiltonian becomes block diagonal in the charge and spin degrees of freedom, that is,

$$\hat{H} = \sum_q \left\{ v_F|q| b_\rho^\dagger(q) b_\rho(q) + |q| \left[\frac{g_4}{2\pi} b_\rho^\dagger(q) b_\rho(q) + \frac{g_2}{2\pi} b_\rho^\dagger(q) b_\rho^\dagger(-q) + \text{H.c.} \right] \right\} + \sum_q v_F|q| b_\sigma^\dagger(q) b_\sigma(q), \tag{22}$$

indicating that spin and charge excitations are already separated. A simple Bogoliubov transformation in the charge sector leads to

$$\hat{H} = \sum_q [v_\rho|q| d_\rho^\dagger(q) d_\rho(q) + v_\sigma|q| d_\sigma^\dagger(q) d_\sigma(q)], \tag{23}$$

where two different velocities arise for the final charge density $d_\rho^\dagger(q)$ and spin density $d_\sigma^\dagger(q)$ excitations:

$$v_\rho = \sqrt{\left(v_F + \frac{g_4}{\pi}\right)^2 - \left(\frac{g_2}{\pi}\right)^2} \quad \text{and} \quad v_\sigma = v_F, \tag{24}$$

with v_ρ (v_σ) being the velocity for charge (spin) excitations. This is the standard result found in textbooks [4,5]. The low-energy Hamiltonian $\hat{H}$, shown in Equation (23), is fully separated into spin and charge excitations that have different propagation speeds. The spin excitation, often called spin density wave (SDW), carries spin current but no charge, while the charge excitation, often called charge density wave (CDW), carries charge current but no spin. This phenomenon is highly non-trivial since the two quantum numbers spin and charge that are both carried by one kind of elementary particle are fully dissociated into two independent excitation (spin and charge) modes. The separation between spin and charge is a peculiarity of one-dimensional systems in the absence of spin–orbit coupling and Zeeman fields, but in the presence of interactions. When the interactions are zero $g_4 = g_2 = 0$, the velocities $v_\rho = v_\sigma = v_F$, that is, spin and charge excitations both travel at the Fermi velocity v_F and thus are not separated. The role played by interactions is crucial in separating charge and spin, that is, in creating $v_\rho \neq v_\sigma$. Although spin–charge separation in 1D is a very old topic, there are still several open questions, which are discussed next.

3.2. *Open questions for spin–charge separation*

Spin–charge separation is a fundamental phenomenon in condensed matter physics, which emerges for one-dimensional systems in the low-energy and long-wavelength regime, when spin–orbit coupling and Zeeman fields are absent. So far, to our knowledge, there is no rigorous proof that spin–charge separation occurs at all energies and wavelengths for arbitrary interaction potentials in 1D. This seems to be the case both for continuum and lattice systems. Furthermore, we are not aware of Bethe-Ansatz-type solutions that prove spin–charge separation for an arbitrary interaction, for either continuum or lattice models in 1D. Therefore, the question "Does spin–charge separation exist for 1D fermions at all energies, wavelengths and arbitrary interaction potentials either in the continuum or in the lattice?" does not seem to have yet a rigorous answer, and thus appears to be an open question[1].

[1] This statement was triggered by a question that Yvan Castin asked, regarding C. A. R. Sá de Melo's presentation at the Institut Henri Poincaré, wondering if spin–charge separation in 1D is only a low-frequency-long-wavelength result or a more general property.

However, based on the Bethe Ansatz, it seems that a rigorous answer to the less general question "Is there spin–charge separation for a zero-ranged potential in the 1D continuum?" is now known theoretically [76]. While, Bethe-Ansatz solutions for the ground state energy for contact (delta function) potential were explored by Yang [77] and Gaudin [78] long ago, it was not until very recently that the charge and spin excitation spectra of such model system were obtained [76]. Not long after these recent theoretical results, experiments claiming the observation of spin–charge separation in ^{6}Li emerged [16], but with some additional harmonic confinement. It would be quite interesting to have experimental measurements of dynamical structure factors in 1D box potentials to further verify the existence of spin and charge density modes propagating with different velocities.

The related question "Is there spin–charge separation for the Hubbard model in the 1D lattice?" appears to be still open. In the Tomonaga–Luttinger regime of the 1D Hubbard model, spin–charge separation is well established [4], and in the limit of $U \to \infty$, a Bethe Ansatz analysis suggests that spin–charge separation remains [79]. However, to our knowledge, there is no Bethe-Ansatz solution that provides the answer to this question for arbitrary U. Nevertheless, there seems to be recent experimental evidence that spin–charge separation occurs in strongly correlated 1D conductors [80], which should stimulate the search for Bethe-Ansatz solutions for arbitrary values of $U > 0$ in the 1D Hubbard model.

In the absence of very general results, the separation between spin and charge in 1D was discussed above in the low-energy and long-wavelength regime, for finite ranged interactions, but without spin–orbit coupling and Rabi fields. However, an arbitrary small amount of SOC and Rabi fields couple charge and spin excitations in SU(2) (spin-1/2) and produce more exotic collective modes that we call Weyl bosons, as we discuss next.

4. SU(2) fermions with SOC and Rabi fields

Fermions with two internal states, attractive interactions, SOC and Rabi fields have been studied theoretically in 3D [81–86], as well as in 2D [87,88] both at zero and finite temperatures, where the focus was on superfluid properties. On the experimental side, a few ultracold Fermi systems with SOC were preliminarily explored such as ^{6}Li [38], ^{40}K [89] and ^{173}Yb [39,68]. Here, we discuss fermions with two internal states, repulsive interactions, SOC and Rabi fields in 1D, and make direct connections to spin–charge separation in the absence of spin–orbit and Rabi couplings and to the special mixing of spin and charge when SOC and Rabi fields are present.

Our discussion about spin-1/2 fermions with SOC and Rabi fields in 1D begins from the experimentally realized Hamiltonian matrix in momentum space with kinetic, SOC and Rabi/Zeeman terms discussed in Equation (11) by setting the detuning δ to zero:

$$\hat{H}_{\rm KS} = \epsilon_k I - h_x \sigma_x - h_z(k)\sigma_z. \tag{25}$$

Here, k is the momentum along the real space x direction, $\epsilon_k = (k^2 + k_T^2)/2m$ is the shifted kinetic energy, k_T is the magnitude of the momentum transferred, h_x is the Rabi field, and $h_z(k) = kk_T/m$ is the momentum-dependent Zeeman field representing the SOC. Notice that, for our 1D system, the SOC is the equal Rashba and Dresselhaus (ERD) type discussed in Section 2.1 and shown in Equation (8). In our 1D analysis, we converted the notation used in Equation (11) via the following prescription: $\mathbf{k} \to k\mathbf{e_x}$, $\delta \to 0$, $\Omega/2 \to h_x$, and $\mathbf{k_T}\cdot\mathbf{k}/m \to kk_T/m = h_z(k)$. This notation highlights the role played by h_x and $h_z(k)$ as a uniform Zeeman field along the spin-space x direction and a momentum-dependent Zeeman field along spin-space z direction, respectively.

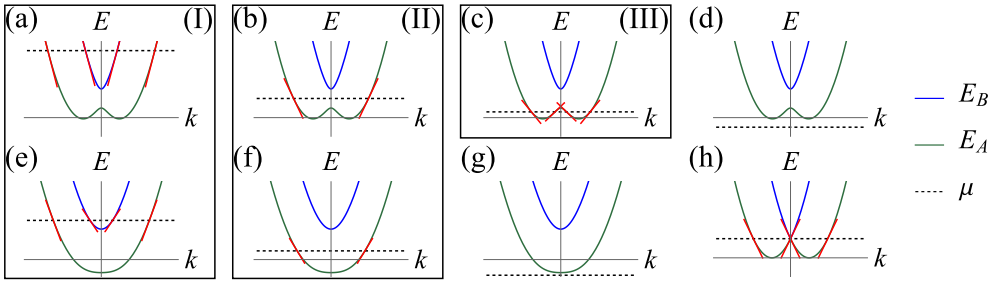

Figure 2. Schematic plots of $E_A(k)$ (green solid line) and $E_B(k)$ (blue solid line) showing effects of SOC (k_T) and Rabi fields (h_x). The red solid lines are linearizations around Fermi points, and the horizontal black dashed lines indicate the chemical potential μ. In panels (a), (b), (c) and (d), $E_A(k)$ has double minima, since $|h_x|/E_T < 2$. In panels (e), (f), and (g), $E_A(k)$ has a single minimum, since $|h_x|/E_T \geq 2$. In panel (h), $h_x = 0$, and the system is equivalent to no SOC due to the spin-gauge symmetry. We show relevant linearizations inside the boxes. Case (I), with four Fermi points, is displayed in panels (a) and (e). Case (II), with two Fermi points, is displayed in panels (b) and (f). Case (III), with four Fermi points, is displayed in panel (c). The Roman numeral in the top-right corner of each box indicates the associated linearization.

We diagonalize the Hamiltonian matrix $\hat{H}_{\rm KS}$ via the momentum-dependent SU(2) rotation matrix

$$U(k,k_T,h_x)=\begin{pmatrix}\cos[\theta(k,k_T,h_x)/2] & -\sin[\theta(k,k_T,h_x)/2]\\ \sin[\theta(k,k_T,h_x)/2] & \cos[\theta(k,k_T,h_x)/2]\end{pmatrix}, \tag{26}$$

where the SU(2) rotation angle

$$\theta(k,k_T,h_x)=2\arctan\left[\frac{h_z(k)-h_{\rm eff}(k)}{h_x}\right]=\arctan\left[-\frac{h_x}{h_z(k)}\right] \tag{27}$$

depends on momentum k, the SOC parameter k_T via $h_z(k)$, and the Rabi field h_x. The resulting dispersions of the energy eigenvalues are

$$E_A(k)=\epsilon_k-h_{\rm eff}(k) \quad \text{and} \quad E_B(k)=\epsilon_k+h_{\rm eff}(k), \tag{28}$$

where $h_{\rm eff}(k)=\sqrt{h_x^2+h_z^2(k)}$ plays the role of a momentum-dependent Zeeman field. The creation operators in the energy eigenbasis are

$$\left(a_A^\dagger(k)\ a_B^\dagger(k)\right)=\left(c_\uparrow^\dagger(k)\ c_\downarrow^\dagger(k)\right)U^\dagger(k), \tag{29}$$

where $c_s^\dagger(k)$ are the creation operators with momentum k and spin $s=\{\uparrow,\downarrow\}$. The operators $a_\alpha^\dagger(k)$ create helical fermions, because the matrix $U(k)$ has an SU(2) momentum-dependent rotation angle $\theta(k,k_T,h_x)$ induced by SOC when both k_T and h_x are non-zero. Thus, the diagonalized kinetic energy operator in second quantization is

$$\hat{H}_{\rm kin}=\sum_{k\alpha}E_\alpha(k)a_\alpha^\dagger(k)a_\alpha(k). \tag{30}$$

In Figure 2, we show $E_A(k)$ and $E_B(k)$ in various situations [90]. When $h_x\neq 0$, the eigenvalues $E_A(k)$ and $E_B(k)$ are non-degenerate with $E_A(k)$ having either double minima ($|h_x|<2E_T$), revealed in Figure 2(a,b,c,d), or a single minimum ($|h_x|\geq 2E_T$) displayed in Figure 2(e,f,g), where $E_T=k_T^2/2m$. When $h_x=0$, we have $h_{\rm eff}(k)=|h_z(k)|$ and the two bands intersect at $k=0$, as shown in Figure 2(h).

A natural question that arises is: How is the SOC-induced helicity of the fermions transferred to the low-energy excitations of the interacting problem? To answer this question, we need to investigate the effects of SOC on the interaction part of the Hamiltonian.

Since, in this section, we are interested in spin-1/2 cold atom systems, we model interactions for two-internal-state ^{6}Li, ^{40}K or ^{173}Yb as

$$\hat{H}_{\rm int} = V_0 \int_0^{L_b} {\rm d}x' \int_0^{L_b} {\rm d}x \hat{n}_\uparrow(x)\hat{n}_\downarrow(x') f(|x-x'|), \tag{31}$$

where L_b is the length of system, $\hat{n}_s(x) = \psi_s^\dagger(x)\psi_s(x)$ is the local density operator with spin label $s = \{\uparrow, \downarrow\}$. The interaction in Equation (31) is SU(2) invariant and spin-dependent like the general case mentioned in Equation (15) of Section 3. The dimensionless function $f(|x-x'|)$ controls the range R_0, and the parameter V_0, possessing energy dimensions, controls the strength of interactions. A transformation to momentum space yields

$$\hat{H}_{\rm int} = \frac{V_0}{L_b} \sum_q \hat{\rho}_\uparrow(q)\hat{\rho}_\downarrow(-q)\tilde{f}(q), \tag{32}$$

where $\hat{\rho}_s(q) = \sum_k c_s^\dagger(k)c_s(k+q)$ is the Fourier transform of the local density operator $\hat{n}_s(x)$, and $\tilde{f}(q) = \int {\rm d}y {\rm e}^{-{\rm i}qy} f(|y|)$, with dimensions of length, is the Fourier transform of the dimensionless function $f(|y|)$. Since any finite-ranged real space interaction leads to the same low-energy and long-wavelength effective interaction, we choose the dimensionless function to be the Gaussian $f(|y|) = 1/\sqrt{2\pi}\exp -y^2/2R_0^2$. The Fourier transform of $f(|y|)$, shown in Equation (32), is $\tilde{f}(q) = R_0 \exp -q^2R_0^2/2$, having dimensions of length. The application of this approach to specific ultracold fermions (^{6}Li,^{40}K,^{173}Yb) is discussed later.

When $h_x = 0$, the spin-gauge transformation $\psi_\uparrow(x) \to {\rm e}^{{\rm i}k_T x}\psi_\uparrow(x)$, $\psi_\downarrow(x) \to {\rm e}^{-{\rm i}k_T x}\psi_\downarrow(x)$ gauges away k_T in the kinetic energy without changing the interaction $\hat{V}$ (spin-gauge symmetry). However, when both $k_T \neq 0$ and $h_x \neq 0$, the interaction written in the basis of eigenstates of the kinetic energy operator with SOC and Rabi fields acquires a much more complex structure controlled by the unitary transformation $U(k)$ that connects $\left(a_A^\dagger(k)\ a_B^\dagger(k)\right)$ and $\left(c_\uparrow^\dagger(k)\ c_\downarrow^\dagger(k)\right)$. The bosonization procedure must be performed in the eigenbasis $\left(a_A^\dagger(k)\ a_B^\dagger(k)\right)$ of the kinetic energy operator $\hat{H}_{\rm int}$ and not in the starting basis $\left(c_\uparrow^\dagger(k)\ c_\downarrow^\dagger(k)\right)$, as discussed next.

4.1. *Bosonization with SOC and Rabi fields*

To describe low-energy excitations of the total Hamiltonian $\hat{H} = \hat{H}_{\rm kin} + \hat{H}_{\rm int}$, we use the bosonization technique presented in Section 3.1 and linearize the kinetic energy operator $\hat{H}_{\rm kin}$ in Equation (30) around the chemical potential μ for each energy dispersion $E_A(k)$ and $E_B(k)$, given in Equation (28). Linearization is only possible when $\mu > \min\{E_A(k), E_B(k)\}$. However, the linear-spectrum approximation is strictly valid only in the low-energy regime near the Fermi points where curvature effects are negligible. When the Fermi velocities are non-zero, the curvature of the dispersions are a second-order effect. A treatment of nonlinear (band-curvature) corrections, without spin–orbit coupling and Rabi fields, can be found in the literature [91]. For $h_x \neq 0$ and arbitrary k_T, there are three typical linearization cases shown in Figure 2: (I) μ intersects twice $E_A(k)$ and twice $E_B(k)$, see Figures 2(a,e); (II) μ intersects only $E_A(k)$ twice, see Figures 2(b,f); (III) μ intersects $E_A(k)$ four times, see Figure 2(c). When $\mu < \min\{E_A(k), E_B(k)\}$, μ does not intersect either $E_A(k)$ or $E_B(k)$, thus no linearization is possible, see Figure 2(d,g). The special situation of $h_x = 0$ and arbitrary k_T is shown in Figure 2(h). Intersections of μ to either $E_A(k)$ or $E_B(k)$ allows for linearization of dispersions, shown as red lines in Figure 2.

We label fermions via indices $\{r, \alpha\}$, where r describes left (L) or right (R) moving particles and α labels the band indices A or B indicating linearization of $E_A(k)$ or $E_B(k)$. In the special case of Figure 2(c), we set $\alpha = A^{(1)}$ for the outer red lines and $\alpha = A^{(2)}$ for the inner red lines, since only $E_A(k)$ is crossed by μ. The linearized kinetic energy operator is

$$\hat{H}_{\rm kin} = \sum_{k\alpha r} \{\mu + {\rm sgn}(r)u_\alpha[k - {\rm sgn}(r)k_{\mu\alpha}]\} a_{\alpha r}^\dagger(k)a_{\alpha r}(k), \tag{33}$$

where u_α is the Fermi velocity $\mathrm{d}E_\alpha(k)/\mathrm{d}k$ at $k = k_{\mu\alpha}$, with $k_{\mu\alpha}$ being the positive momentum where μ intersects the band labeled by α. The operator $a^\dagger_{\alpha r}(k)$ creates a fermion with momentum k in band α and branch r. Both u_α and $k_{\mu\alpha}$ depend on k_T, h_x and μ. The function $\mathrm{sgn}(r)$ refers to the sign of r, where $\mathrm{sgn}(R) = +1$ and $\mathrm{sgn}(L) = -1$. The reference Hamiltonian $\hat{H}_0 = \sum_{k\alpha r} \mu a^\dagger_{\alpha r}(k) a_{\alpha r}(k)$, corresponding to the energy $E_0 = N\mu$, where N is the total number of fermions, is set to zero without loss of generality. Thus, we drop this reference term from the kinetic energy operator $\hat{H}_{\rm kin}$ from now on.

We bosonize $\hat{H}_{\rm kin}$ in Equation (33) using the transformation

$$b^\dagger_\alpha(q) = \sqrt{\frac{2\pi}{|q|L_b}} \sum_r \Theta(-\mathrm{sgn}(r)q)\hat{\rho}_{\alpha r}(q), \tag{34}$$

where $\hat{\rho}_{\alpha r}(q) = \sum_k a^\dagger_{\alpha r}(q) a_{\alpha r}(k+q)$ is the fermion density operator for an r-moving particle in band α, and $\Theta(x)$ is the Heaviside step function. This leads to

$$\hat{H}_{\rm kin} = \sum_{q\alpha} |q u_\alpha| b^\dagger_\alpha(q) b_\alpha(q) + K_\Omega \tag{35}$$

for the kinetic energy in bosonized form, where $K_\Omega = \sum_{q>0,\alpha} |q u_\alpha|$. Here, the bosonization of the interaction is more complex because it requires four sets of momentum-dependent unitary transformations, when writing the interaction Hamiltonian in terms of the creation $a^\dagger_A, a^\dagger_B$ and annihilation a_A, a_B operators. Using the appropriate momentum labels, the interaction in Equation (32) is bosonized as

$$\hat{H}_{\rm int} = \sum_{q>0} q\mathbf{\Phi}^\dagger(q) g \mathbf{\Phi}(q) = \frac{1}{2}\sum_q |q| \mathbf{\Phi}^\dagger(q) g \mathbf{\Phi}(q) + V_\Omega, \tag{36}$$

where $\mathbf{\Phi}(q)$ is either a two-component vector or a four-component vector, g is either a 2×2 or a 4×4 matrix representing the interaction strength of different scattering processes shown in Figure 3, and $V_\Omega = \sum_{qij} |q| g_{ij}/2$, with g_{ij} being the elements of the matrix g. In case (I), where μ intersects bands A and B, there are four Fermi points, and

$$\mathbf{\Phi}^T(q) = \left(b^\dagger_A(q)\ b^\dagger_B(q)\ b_A(-q)\ b_B(-q)\right).$$

In case (II), where μ intersects only band A, there are two Fermi points, and $\mathbf{\Phi}^T(q) = \left(b^\dagger_A(q)\ b_A(-q)\right)$. In case (III), where μ intersects only band A, there are four Fermi points, and

$$\mathbf{\Phi}^T(q) = \left(b^\dagger_{A^{(1)}}(q)\ b^\dagger_{A^{(2)}}(q)\ b_{A^{(1)}}(-q)\ b_{A^{(2)}}(-q)\right).$$

The elements of the g matrix are $g_{ij} = \eta_{ij}\tilde{f}(q\to 0)$, having dimensions of energy times length, while η_{ij} has dimension of energy and depends on k_T, h_x and μ via SU(2) rotation angles $\theta(k, k_T, h_x)$ and $\theta(k+q, k_T, h_x)$.

For case (I), the g matrix is 4×4 and depends on the angles θ_A and θ_B, where $\theta_\alpha = \theta(k_{\mu\alpha}, k_T, h_x)$ is the SU(2) angle defined in Equation (27) with $k = k_{\mu\alpha}$. For case (II), the g matrix is 2×2 and depends only on θ_A as

$$g = \frac{\tilde{f}(0)V_0}{4\pi}\begin{pmatrix} \sin^2\theta_A & (1+\cos^2\theta_A) \\ (1+\cos^2\theta_A) & \sin^2\theta_A \end{pmatrix}. \tag{37}$$

For case (III), the g matrix is 4×4 and depends on the SU(2) angles $\theta_{A^{(1)}}$ and $\theta_{A^{(2)}}$. The g matrix in cases (I) and (III) can also be obtained analytically [92], but for simplicity and brevity, we discuss in detail only case (II) as an example [92]. In general, $g_{4\alpha\beta}$ ($g_{2\alpha\beta}$) shown in Figure 3 are the diagonal (off-diagonal) terms of each 2×2 block of the g matrix, where the blocks are labeled by α, β. For instance, in case (II), $g_{4AA} = (\tilde{f}(0)V_0/4\pi)\sin^2\theta_A$ are the diagonal and $g_{2AA} = (\tilde{f}(0)V_0/4\pi)(1+\cos^2\theta_A)$ are the off-diagonal elements of matrix g in Equation (37).

Only small momentum-transfer interactions ($q\to 0$) are retained, since larger momentum-transfer contributions $q = 2k_{\mu\alpha}$ are suppressed due to the finite range R_0 of the interaction,

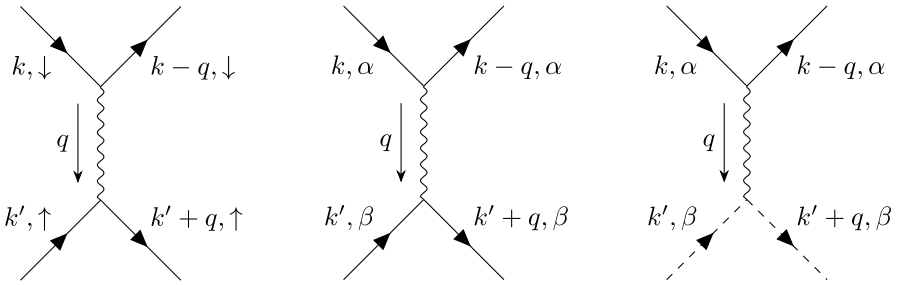

Figure 3. Schematics of scattering processes. In panel (a), we show the scattering process in the spin basis $\{\uparrow,\downarrow\}$. In panels (b) and (c), we show the low-momentum-transfer scattering processes in the $\{\alpha,\beta\}$ basis after linearization, where $\{\alpha,\beta\}=\{A,B\}$ for case (I), $\{\alpha,\beta\}=\{A\}$ for case (II), and $\{\alpha,\beta\}=\{A^{(1)},A^{(2)}\}$ for case (III). The solid (dashed) lines represent right (left) moving fermions, and the wiggly lines represent the interactions.

and even when these terms are included they are irrelevant under the renormalization group flow [4,6,92]. This is an important point in our discussion, because we use a finite-ranged interaction. As an example, for the Gaussian-ranged interaction, $\tilde{f}(0)=R_0$. The limit of zero interaction range is discussed later, when connections to ultracold atoms are directly made. The bosonized Hamiltonian is now ready for diagonalization, as discussed next.

4.2. *Diagonalization of bosonized Hamiltonian*

To obtain the excitation spectrum of the bosonized Hamiltonian

$$\hat{H}=\hat{H}_{\rm kin}+\hat{H}_{\rm int},$$

it is necessary to diagonalize it via a Bogoliubov transformation $\mathscr{B}$ connecting $\mathbf{\Phi}(q)$ in Equation (36) to $\mathbf{\Psi}(q)=\mathscr{B}\mathbf{\Phi}(q)$, leading to boson operators

$$\mathbf{\Psi}^T(q)=\left(d_1^\dagger(q)\ d_2^\dagger(q)\ d_1(-q)\ d_2(-q)\right)$$

for cases (I) and (III), where the number of collective modes is $N_{\rm C}=2$ and to $\mathbf{\Psi}^T(q)=\left(d_1^\dagger(q)\ d_1(-q)\right)$ for case (II), where $N_{\rm C}=1$. Barring any instabilities, $N_{\rm C}=N_{\rm F}/2$, where $N_{\rm F}$ is the number of Fermi points at μ. The Bogoliubov matrices $\mathscr{B}$ are 4×4 in cases (I) and (III) and 2×2 in case (II). This is a very standard procedure, so we do not dwell on the details. After implementing the Bogoliubov transformations, the diagonalized Hamiltonian becomes

$$\hat{H}=\sum_{q\ell}|q|v_\ell d_\ell^\dagger(q)d_\ell(q)+\omega_\Omega, \tag{38}$$

where $v_\ell\geq0$ is the velocity of collective mode ℓ that depends on $\{k_T,h_x,\mu\}$ for given V_0. The ground state energy is $\omega_\Omega=\sum_{q>0,\ell}|qv_\ell|$. Defining $\mathscr{L}$ to be the set of collective modes, such that $\ell\in\mathscr{L}$, we have two modes for cases (I) and (III) with $\mathscr{L}=\{1,2\}$, and we have one mode for case (II) with $\mathscr{L}=\{1\}$. The mode with $\ell=1$ has larger velocity and energy, while the mode with $\ell=2$ has smaller velocity and energy. The velocities v_ℓ can be obtained analytically, but have complicated expressions in cases (I) and (III) [92]. For simplicity and brevity, we give analytical results only for case (II), see Figures 2(b) and (f), where there is only one mode with velocity

$$v_1=\sqrt{u_A+\frac{\tilde{f}(0)V_0}{2\pi}}\sqrt{u_A-\frac{\tilde{f}(0)V_0}{2\pi}\cos^2\theta_A}. \tag{39}$$

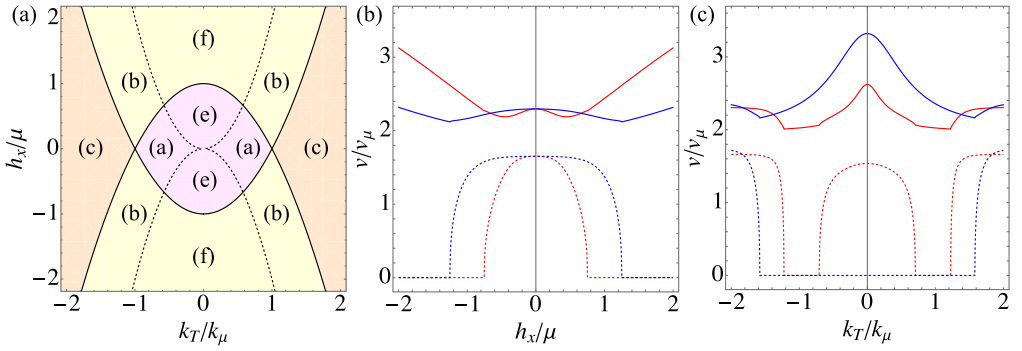

Figure 4. Phase diagram and velocities of collective modes. In panel (a), we show the phase diagram of h_x/μ versus k_T/k_μ, for chemical potential $\mu > 0$ and $k_\mu = \sqrt{2m\mu}$. The interaction parameter is chosen to be $\tilde{f}(0)V_0/v_\mu = 2$, where $v_\mu = k_\mu/m$. The pink, yellow and orange regions represent phases with four (two), two (one), and four (two) Fermi points (collective modes). These phases are separated by black solid lines, where topological quantum phase (Lifshitz) transitions occur. The labels (a) and (e) in the pink region, (b) and (f) in the yellow region, and (c) in the orange region refer to the cases illustrated in the panels of Figure 2. The black dashed lines at $|h_x| = 2E_T$ separate regions where $E_A(k)$ has a single minimum ($|h_x|/E_T > 2$) from regions where $E_A(k)$ has double minima ($|h_x|/E_T < 2$). In panel (b), we show the velocities v_1/v_μ (solid lines) and v_2/v_μ (dashed lines) as functions of h_x/μ for fixed values of k_T/k_μ. The red curves correspond to $k_T/k_\mu = 0.5$, and the blue curves to $k_T/k_\mu = 1.5$. In panel (c), we show the velocities v_1/v_μ (solid lines) and v_2/v_μ (dashed lines) as functions of k_T/k_μ for fixed values of h_x/μ. The red curves correspond to $h_x/\mu = 0.5$, and the blue curves to $h_x/\mu = 1.5$.

In the expression above, for $h_x \neq 0$ and $k_T \neq 0$, the Fermi velocity is

$$u_A = \left(1 - \frac{2E_T}{h_{\rm eff}(k_{\mu A})}\right)\frac{k_{\mu A}}{m}, \tag{40}$$

where $E_T = k_T^2/2m$ is the momentum-transfer energy, $h_{\rm eff}(k_{\mu A}) = \sqrt{h_x^2 + h_z^2(k_{\mu A})}$ is the effective Zeeman field at $k_{\mu A}$ with $h_z(k_{\mu A}) = k_{\mu A}k_T/m$ being the momentum-dependent Zeeman field, and with

$$k_{\mu A} = \sqrt{2m(\mu + E_T + \sqrt{4\mu E_T + h_x^2})} \tag{41}$$

being the Fermi momentum for band A.

In Figure 4, we illustrate properties of our system in the plane h_x/μ versus k_T/k_μ, with $\mu > 0$ and $k_\mu = \sqrt{2m\mu}$. Panel (a) shows a partial phase diagram for $\mu > 0$. Panel (b) displays the velocities v_ℓ/v_μ of collective modes with $\ell = 1,2$ as a function of h_x/μ at fixed k_T/k_μ. Panel (c) reveals the velocity v_ℓ/v_μ of collective modes with $\ell = 1,2$ as a function of k_T/k_μ at fixed h_x/μ. We fix the chemical potential μ and, for simplicity, show only the case of $\mu > 0$, instead of fixing the density n as was discussed in the literature [90].

In Figure 4(a), we show the phase diagram of h_x/μ versus k_T/k_μ, for $\mu > 0$, with $k_\mu = \sqrt{2m\mu}$, and $\tilde{f}(0)V_0/v_\mu = 1$, where $v_\mu = k_\mu/m$. Case (I), where μ intersects bands A and B as shown in Figure 2(a,e), is represented by the pink region, with the number of Fermi points $N_{\rm F} = 4$ and the number of collective modes $N_{\rm C} = 2$. Case (II), where μ intersects only band A twice, as seen in Figure 2(b,f), is represented by the yellow region with $N_{\rm F} = 2$ and $N_{\rm C} = 1$. Case (III), where μ intersects only band A four times as shown in Figure 2(c), is represented by the orange region with $N_{\rm F} = 4$ and $N_{\rm C} = 2$. For the vertex separating the pink, yellow and orange regions ($h_x/\mu = 0$

and $k_T/k_\mu = 1$), $N_F = 4$ as in Figure 2(h) and $N_C = 2$; at this location there is perfect spin–charge separation. In fact, along the line $h_x/\mu = 0$, there is spin–charge separation also in the pink and orange regions, due to the spin-gauge symmetry.

Furthermore, in Figure 4(a), the lines or points separating different phases indicate topological quantum phase transitions of the Lifshitz-type [93–95], where the Fermi *surfaces* change from four to two to zero points, depending on h_x/μ and k_T/k_μ. The black dashed lines (parabolas) at $h_x = \pm 2E_T$ separate regions where the lower band $E_A(k)$ has two minima ($|h_x| < 2E_T$) from regions where the lower band $E_A(k)$ has one minimum ($|h_x| > 2E_T$) and the line at $h_x/\mu = 0$ represents the locus of spin–charge separation.

In Figure 4, we also show the collective mode velocities v_1/v_μ and v_2/v_μ, where $v_\mu = k_\mu/m$, as a function of h_x/μ and fixed k_T/k_μ in panel (b) or as a function of k_T/k_μ for fixed h_x/μ in panel (c). Solid and dotted curves represent v_1/v_μ and v_2/v_μ, respectively. In panel (b), the red curves correspond to $k_T/k_\mu = 0.5$, and the blue curves to $k_T/k_\mu = 1.5$; in panel (c), the red curves correspond to $h_x/\mu = 0.5$, and the blue curves to $h_x/\mu = 1.5$. Both v_1/v_μ and v_2/v_μ vary continuously but exhibit nonanalytic behavior at phase boundaries (black solid lines in panel (a)). This nonanalyticity reflects a topological (Lifshitz) quantum phase transition, characterized by a change in the number of Fermi points from $N_F = 4$ to $N_F = 2$. Additionally, at the phase boundaries, the velocity of the second mode vanishes. This results from the linearization, where the slope at a local maximum or minimum becomes zero. To obtain the next order correction to the collective mode dispersion, it is necessary to include curvature effects as described in Ref. [91]. However, we do not address the additional correction in this paper.

We notice that, in the limit $h_x/\mu \to 0$ for fixed nonzero k_T/k_μ, the velocities approach their theoretical values at $h_x/\mu = 0$ due to spin-gauge symmetry, thereby restoring spin–charge separation. When spin–charge separation happens at $h_x = 0$, the higher-velocity mode (v_1) is associated with charge and the lower-velocity mode (v_2) is associated with spin. In the absence of SOC ($k_T = 0$) with $h_x \neq 0$, the collective modes are generally a mix of charge and spin density waves, but are nonhelical. However, when both $k_T \neq 0$ and $h_x \neq 0$, the collective modes are a mix of charge and spin density waves with a helical structure, which is carried over by the momentum-dependent rotation angles $\theta(k, k_T, h_x)$ of the SU(2) rotation matrices $U(k)$ defined in Equation (26).

To visualize helical modulations in the collective modes, we decompose

$$d^\dagger_\ell(q) = \sum_r \left[A_{\ell r}(q)\hat{\rho}_r(q) + \mathbf{B}_{\ell r}(q)\cdot\hat{\mathbf{s}}_r(q)\right] \tag{42}$$

in terms of the Fourier transforms $\hat{\rho}_r(q)$ and $\hat{\mathbf{s}}_r(q)$ of the charge-density $\hat{n}_r(x) = \sum_s \psi^\dagger_{sr}(x)\psi_{sr}(x)$ and spin-density $\hat{\mathbf{S}}_r(x) = \frac{1}{2}\sum_{ss'}\psi^\dagger_{sr}(x)(\boldsymbol{\sigma})_{ss'}\psi_{s'r}(x)$ operators, respectively. Here, the factor of $1/2$ in $\hat{\mathbf{S}}_r(x)$ represents the angular momentum $\hbar/2$ with $\hbar = 1$, r labels right (R) or left (L) going fermions, and $\psi^\dagger_{sr}(x)$ is the creation operator for r-going fermions with spin projection s at position x. The collective mode operators in real space are

$$\mathscr{D}^\dagger_\ell(x) = \sum_r \int \mathrm{d}x' \left[a_{\ell r}(x-x')\hat{n}_r(x') + \mathbf{b}_{\ell r}(x-x')\cdot\hat{\mathbf{S}}_r(x')\right], \tag{43}$$

where the spatial modulation and helicity of the vector fields $\mathbf{b}_{\ell r}(x-x')$ are controlled by k_T and h_x [90,92]. When k_T and h_x are both non-zero, all the modes present are helical, with $q > 0$ ($q < 0$) modes having positive (negative) helicity. The global helicity of the Hamiltonian in Equation (38) is zero, such that $q > 0$ and $q < 0$ bosons for each mode are helical pairs. Given that these bosons are massless and helical, we name them Weyl bosons in analogy to Weyl fermions [50], which are massless and helical spin-1/2 particles. The helicity of Weyl bosons is like that of circularly polarized photons, however unlike photons, in SU(2) Fermi systems, Weyl bosons can have up to two flavors of right or left helicities. We emphasize that our flavored Weyl bosons

are collective modes of interacting and spin–orbit-Rabi-coupled spin-1/2 fermions. They are intrinsically *pseudo-relativistic* (*relativistic*) bosons due the presence of synthetic (real) Zeeman fields and synthetic (real) spin–orbit coupling that provides *relativistic* corrections. They also appear in 2D and 3D, but in 1D, analytical results are easily obtained via the bosonization method. We also notice that the emergence of Weyl bosons in the context of particle physics corresponds to an effect Beyond the Standard Model (BSM), thus the analysis above offers some hope for those interested in simulating BSM effects with ultracold atoms.

The theoretical results described above need serious experimental testing, thus we discuss next potential experimental systems that may reveal the existence of Weyl bosons.

4.3. *Connection to ultracold Fermi atoms*

For ultracold fermions such as ^{6}Li, ^{40}K and ^{173}Yb, with two internal states selected and SU(2) invariant interactions, the zero-range approximation is typically used. Thus, the effective zero-ranged interaction is replaced by the scattering length. To take the limit of zero range ($R_0 \to 0$), we use the explicit Gaussian form $f(|y|) = 1/\sqrt{2\pi}\exp -y^2/2R_0^2$, discussed right after Equation (32) and connect it to the delta sequence $\delta_n(y) = (n/\sqrt{2\pi})\exp(-n^2y^2/2)$. With this connection, we write the 1D interaction

$$V(x-x') = V_0 f(|x-x'|), \tag{44}$$

with range R_0, in the limit of $R_0 \to 0$, as the contact potential

$$V(x-x') \approx \widetilde{V}_0 \delta(x-x'), \tag{45}$$

where $\widetilde{V}_0 = R_0 V_0$, with dimensions of energy times length, is held constant as $R_0 \to 0$. Notice that $\widetilde{V}_0$ is also equivalent to $\tilde{f}(0)V_0$ discussed in the previous sections, where $\tilde{f}(0) = R_0$. The corresponding 1D scattering length a_{1D} is defined by the relation $\widetilde{V}_0 = -2\hbar^2/ma_{1D} > 0$ (with $\hbar$ restored to make units clear) [96]. The relationship between a_{1D} and the 3D scattering length a_{3D} is [16,96]

$$a_{1D} = -\frac{a_\perp}{a_{3D}}\left[1 - C\frac{a_{3D}}{a_\perp}\right], \tag{46}$$

where $C = |\zeta(1/2)|/\sqrt{2}$ is a constant with $\zeta(1/2)$ being the Riemann zeta function $\zeta(z)$ evaluated at $z = 1/2$, and $a_\perp = \sqrt{\hbar/m\omega_r}$ is the transverse confinement length with ω_r being the frequency of the transverse harmonic potential [96].

Given that ^{6}Li experiences substantial heating due to the Raman beams [38] that produce SOC and Rabi fields, the effects proposed above are more likely realizable in ^{40}K or ^{173}Yb. So, we choose to give numbers compatible with ^{40}K as an illustration, since typical SOC and Rabi fields are known [89]. We envision using optical boxes in 1D with dimensions ranging from 10 μm to 100 μm [97], and number of atoms varying from a few [98] to thousands [99]. As an example, we consider a 1D optical box with length $L_b = 25$ μm, a tight transverse confinement frequency $\omega_r = 2\pi \times 227.5$ kHz, similar to confinements achieved in ^{6}Li [16], number of atoms $N = 400$, interaction parameter $\widetilde{V}_0 = R_0 V_0 = v_\mu$ in the zero-range limit $R_0 \to 0$. For ^{40}K, the momentum transfer chosen is $k_T = 2\pi \times (768.86\ \text{nm})^{-1}$ [89], the density is $n = 400/25\ \mu\text{m} = 1.6 \times 10^5/\text{cm}$, and the 3D scattering length from Equation (46) is $a_{3D} \approx 134 a_0$, where a_0 is the Bohr radius. Other examples can be found in the literature [90].

Keeping in mind this connection to ultracold atoms, we discuss next the dynamical structure factor tensor, which can potentially be measured using Bragg scattering techniques to detect the dispersion, spectral weight and helicity of the collective modes that we call Weyl bosons.

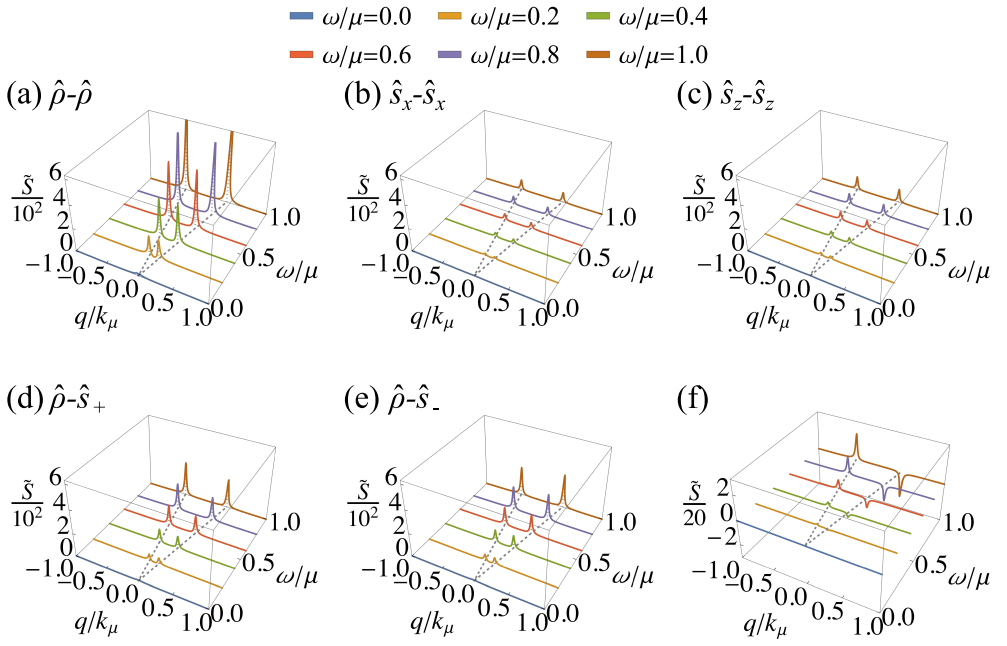

Figure 5. Dimensionless dynamical structure factor (DSF) tensor $\widetilde{S}_{ij}(q,\omega) = S_{ij}(q,\omega)\mu/k_\mu^2$, with energy broadening $\delta/\mu = 0.05$. The parameters used are $h_x/\mu = 1.5$ for the Rabi field, $k_T/k_\mu = 0.5$ ($E_T/\mu = 0.25$) for the SOC, $\widetilde{V}_0/v_\mu = \tilde{f}(0)V_0/v_\mu = 2$ ($a_{3D} \approx 134a_0$) for the interaction and $k_\mu L_b = 408.60$. These are typical values for ^{40}K, at density $n = 1.6\times10^5/\text{cm}$, in a 1D box potential of length $L_b = 25$ μm. These parameters correspond to a point in the yellow region of the phase diagram of Figure 4(a) leading to a single collective mode (Weyl boson). Panels (a), (b) and (c) show the charge–charge and spin–spin responses $\hat{\rho}$-$\hat{\rho}$, $\hat{s}_x$-$\hat{s}_x$ and $\hat{s}_z$-$\hat{s}_z$, respectively. Panels (d) and (e) display the charge–spin $\hat{\rho}$-$\hat{s}_+$ and $\hat{\rho}$-$\hat{s}_-$ responses, respectively, and (f) shows the difference of (d) and (e). The gray dashed lines show the dispersing helical collective mode (Weyl boson).

4.4. *Dynamical structure factor tensor*

Bragg scattering techniques have been used to measure velocities of charge and spin density collective modes [63,64], as well as to identify spin–charge separation [16,17] in ^{6}Li. These experiments traditionally measure either charge or spin dynamical structure factors (DSF). Here, we investigate not only spin–spin and charge–charge, but also spin–charge responses at $T = 0$ via the DSF tensor

$$S_{ij}(q,\omega) = 2\pi\sum_{p\ell}\langle\Omega|\hat{\mathcal{O}}_i(q)|p,\ell\rangle\langle p,\ell|\hat{\mathcal{O}}_j(-q)|\Omega\rangle\,\delta(\omega-\varepsilon_{p\ell}+\omega_\Omega), \tag{47}$$

for the ground state $|\Omega\rangle$, in the Källén–Lehmann spectral representation [100,101]. The operators $\hat{\mathcal{O}}_i(q)$, with $i = \{c,x,y,z\}$, are the charge $\hat{\mathcal{O}}_c(q) = \hat{\rho}(q)$ and spin $\hat{\mathcal{O}}_a(q) = \hat{s}_a(q)$ operators, where $a = \{x,y,z\}$. The eigenstates of the bosonized Hamiltonian $\hat{H}$ given in Equation (38) are $|p,\ell\rangle$ with corresponding eigenenergies $\varepsilon_{p\ell} = |p|v_\ell$, while ω_Ω is the ground state energy discussed following Equation (38). We emphasize that, in our units ($\hbar = 1$), both $\hat{\rho}(q)$ and $\hat{s}_a(q)$ have dimensions of inverse length and $S_{ij}(q,\omega)$ has dimensions of mass; these properties are used in the plots of Figure 5.

To calculate $S_{ij}(q,\omega)$, we use the decomposition $\hat{\mathcal{O}}_i(q) = \hat{\mathcal{O}}_{iR}(q) + \hat{\mathcal{O}}_{iL}(q)$ in Equation (47), and implement the Moore–Penrose inverse [102,103] of Equation (42) to write the operators $\hat{\mathcal{O}}_{ir}(q)$ as a linear combination of the boson creation $d^\dagger_\ell(q)$ and annihilation $d_\ell(-q)$ operators. When $q > 0$, we obtain

$$\hat{\mathcal{O}}_{ir}(q) = \sqrt{\frac{|q|L}{2\pi}} \sum_\ell (F_{ir\ell}(q) d^\dagger_\ell(q) + G_{ir\ell}(q) d_\ell(-q)), \tag{48}$$

where the expression relating $q > 0$ and $q < 0$ is $\hat{\mathcal{O}}_{ir}(-q) = \hat{\mathcal{O}}^\dagger_{ir}(q)$. Currently, there is no simple analytical form of the tensors $F_{ir\ell}(q)$ and $G_{ir\ell}(q)$, so we do not show their complicated structure here, but rather we perform the Moore–Penrose inverse numerically to obtain the matrix elements $\langle \Omega|\hat{\mathcal{O}}_i(q)|p,\ell\rangle$ and $\langle p,\ell|\hat{\mathcal{O}}_j(-q)|\Omega\rangle$. Summation over p in Equation (47) (only the terms with $p = q$ survive) leads to

$$S_{ij}(q,\omega) = \sum_\ell \mathscr{A}_{ij\ell}(q)\delta(\omega - \varepsilon_{q\ell} + \omega_\Omega), \tag{49}$$

where $\mathscr{A}_{ij\ell}(q)$ plays the role of the spectral weight tensor with dimensions of squared-density (squared-length in 1D), $\varepsilon_{q\ell} = |q|v_\ell$ is the collective mode energy, and we set the ground state energy $\omega_\Omega = 0$ as our energy reference in Figure 5. The spectral weight tensor is

$$\mathscr{A}_{ij\ell}(q) = \mathscr{A}_{ij\ell+}(q)\Theta(q) + \mathscr{A}_{ij\ell-}(q)\Theta(-q). \tag{50}$$

where $\mathscr{A}_{ij\ell+}(q) = |q|L\sum_{rr'} G_{ir\ell}(q)G^*_{jr'\ell}(q)$ is the spectral weight for $q > 0$, $\mathscr{A}_{ij\ell-}(q) = |q|L\sum_{rr'} F^*_{ir\ell}(-q)F_{jr'\ell}(-q)$ is the spectral weight for $q < 0$ and $\Theta(q)$ is the Heaviside step function. The spectral weight tensor is even in q obeying the relation $\mathscr{A}_{ij\ell}(-q) = \mathscr{A}_{ij\ell}(q)$, implying that $\mathscr{A}_{ij\ell+}(-q) = \mathscr{A}_{ij\ell-}(q)$.

The symmetry properties obeyed by $\mathscr{A}_{ij\ell}(q)$ are important in establishing the general Onsager reciprocal relation [104,105] satisfied by the DSF tensor

$$S_{ij}(q,\omega,k_T,h_x) = \epsilon_i\epsilon_j S_{ji}(-q,\omega,-k_T,-h_x), \tag{51}$$

where ϵ_i is the parity of operators $\hat{\mathcal{O}}_i(x,t)$ under time-reversal. For $i = c$ (charge density), $\epsilon_i = +1$, and for $i = \{x,y,z\}$ (spin density), $\epsilon_i = -1$. We verified analytically and numerically this fundamental symmetry relation regarding the dynamical structure factor tensor.

In Figure 5, we show matrix elements of the dimensionless DSF tensor $\widetilde{S}_{ij}(q,\omega) = S_{ij}(q,\omega)\mu/k^2_\mu = S_{ij}(q,\omega)/2m$ with energy broadening $\delta/\mu = 0.05$. The parameters used are $h_x/\mu = 1.5$ for the Rabi field, $k_T/k_\mu = 0.5$ ($E_T/\mu = 0.25$) for the SOC, $\widetilde{V}_0/v_\mu = \tilde{f}(0)V_0/v_\mu = 2$ ($a_{3D} \approx 134a_0$) for the interaction, and $k_\mu L_b = 408.60$ corresponding to typical values for ^{40}K with density $n = 400/25$ μm $= 1.6\times10^5$/cm, in a 1D box of length $L_b = 25$ μm. These values represent a point in the yellow region of Figure 4(a), where there is only one collective mode (Weyl boson).

In all panels of Figure 5, the gray dashed lines represent the dispersing helical mode (Weyl boson). We emphasize that both $\hat{\rho}(q)$ and $\hat{s}_a(q)$ have dimensions of inverse length in our units ($\hbar = 1$). We use either the standard index $a = \{x,y,z\}$ for the spin components or $a = \{+,-,z\}$, with + (−) labeling the spin raising (lowering) operator $\hat{s}_+$ ($\hat{s}_-$).

In panel (a), we illustrate the charge–charge response $\hat{\rho}$-$\hat{\rho}$, while in panels (b) and (c) we show the spin–spin response $\hat{s}_x$-$\hat{s}_x$ and $\hat{s}_z$-$\hat{s}_z$. In panels (d) and (e), we display the charge–spin $\hat{\rho}$-$\hat{s}_+$ and $\hat{\rho}$-$\hat{s}_-$ responses, respectively. To reveal the helicity of the modes, we show the difference of $\hat{\rho}$-$\hat{s}_+$ and $\hat{\rho}$-$\hat{s}_-$ in panel (f). Since the difference of $\hat{\rho}$-$\hat{s}_+$ and $\hat{\rho}$-$\hat{s}_-$ is small, we use a different scale to help visualization in (f). We verified that for $h_x \neq 0$ and $k_T = 0$, the modes are non-helical, and that the only non-zero responses are $\hat{\rho}$-$\hat{\rho}$, $\hat{s}_x$-$\hat{s}_x$ and $\hat{\rho}$-$\hat{s}_x$. Furthermore, for $h_x = 0$ and any k_T, there is spin–charge separation, and the only non-zero responses are $\hat{\rho}$-$\hat{\rho}$, and $\hat{s}_z$-$\hat{s}_z$. The Weyl bosons with $q > 0$ and $q < 0$ are helical pairs representing special spin-charged mixed states introduced by SOC and Rabi fields.

Apart from Weyl modes with one flavor illustrated in Figure 5, there are also examples of Weyl modes with two flavors, existing in the pink region of Figure 4(a), which can be found in the literature [90]. Having completed our analysis of what is known about SU(2) fermions with spin–orbit coupling and Rabi fields in 1D, we discuss next a few open questions.

4.5. *Open questions for SU(2) fermions*

Before listing a few open questions for SU(2) fermions in the presence of spin–orbit coupling and Rabi fields, we summarize briefly the main results discussed above. We analyzed the phase diagram and collective modes of interacting one-dimensional SU(2) Fermi systems with spin–orbit and Rabi coupling. We have shown that Lifshitz-type topological quantum phase transitions occur in the plane of spin–orbit versus Rabi coupling, where there are quantum phases with two, one or zero helical collective modes (Weyl bosons) depending on the topology of the Fermi *surface*. We demonstrated that the velocities of the collective modes are continuous, but nonanalytical as topological phase boundaries are crossed. We also identified the locus of spin–charge separation, and demonstrated that, when spin–orbit and Rabi couplings are both non-zero, the collective modes are helical with mixed spin and charge density components. Lastly, we obtained the dynamical structure factor tensor for charge–charge, spin–charge and spin–spin responses, revealing the dispersions, spectral weights and helicities of collective modes (Weyl bosons). These results pave the way for their experimental detection in systems like ^{6}Li, ^{40}K and ^{173}Yb, but there are a few open questions that we present below.

The discussion above highlights exciting predictions about the creation of Weyl bosons and their possible detection in SU(2) Fermi systems not only in solid state materials and ultracold fermions such as ^{6}Li, ^{40}K and ^{173}Yb in one dimensional, but also in two- and three-dimensional systems. The one-dimensional case is quite appealing because analytical results for the collective mode dispersion and velocity are obtained via the bosonization method in the long-wavelength regime. However, as far as we know, there are currently no experiments either in condensed matter with real spin–orbit and Rabi (Zeeman) fields or in ultracold atoms with synthetic spin–orbit and Rabi (Zeeman) fields that probe the effects proposed. So, there are not only open theoretical questions, but also experimental ones, both in the context of condensed matter and ultracold atoms.

In condensed matter, one important open experimental question is: are there solid state materials in one, two or three dimensions, where real spin–orbit coupling and Rabi (Zeeman fields) can be manipulated to probe the expected theoretical phase diagram and the emergence of Weyl bosons with one or two flavors? Can measurements of the charge–charge (density–density) dynamical structure factor be achieved, using for instance, inelastic neutron scattering or inelastic X-ray scattering? Can the spin–spin dynamical structure factor be measured for solid state systems with spin–orbit and Zeeman coupling using techniques such as inelastic neutron scattering, resonant inelastic X-ray scattering, muon spin resonance, and spin-polarized neutron scattering? Are there any techniques that can probe the charge–spin or spin–charge dynamical structure factors to extract the helicity of the collective modes?

In ultracold atoms, there are several open experimental questions. Can spin–orbit and Rabi coupling be realized and studied experimentally in interacting Fermi systems of ^{6}Li, ^{40}K and ^{173}Yb in one, two and three dimensions? Would box trapping potentials help in realizing such systems? If experimental realization is possible, would the tunability of spin–orbit and Rabi fields be sufficient to probe the theoretical phase diagrams and the topological phases transitions predicted? Would Bragg spectroscopy be sufficient for measuring charge–charge (density–density) and spin–spin structure factors and identify Weyl bosons? Is there a technique that can measure

the charge–spin (density–spin) and spin–charge (spin–density) structure factors to elucidate the helicity of the collective modes (Weyl bosons)?

On the theoretical front, we also list a few open questions for interacting SU(2) fermions with spin–orbit and Rabi (Zeeman) coupling. Are there qualitative differences between the collective modes (Weyl bosons) in one, two and three dimensions? What is the interplay between the continuum of excitations and Weyl bosons? What are the lifetimes of Weyl bosons? Are there stable higher-energy helical collective modes in one, two and three dimensions? Are there any fractionalization effects in the charge (density) and spin sectors that arise from spin–orbit and Rabi (Zeeman) coupling beyond the long-wavelength regime?

Although there are many open questions for SU(2) fermions, an inquisitive mind may also wonder about additional generalizations. An intriguing possibility is the investigation of SU(N) fermions such ^{173}Yb and ^{87}Sr in the presence of SOC and Rabi fields, where Fermi liquid properties [60] and color superfluidity were investigated [61] in 3D for SU(3) fermions. Thus, driven by curiosity, we discuss next the effects of SOC and Rabi fields on SU(3) fermions with three internal states, focusing again on one dimensional systems.

5. SU(3) fermions with SOC and Rabi fields

Ultracold atomic physics has emerged as a versatile platform for simulating complex quantum systems due to the high degree of control over atomic interactions and internal degrees of freedom. Particularly, fermionic atoms with multiple internal states can emulate and break higher symmetries beyond the conventional SU(2) spin symmetry as discussed in Section 4. In this context, SU(3) fermions, with three internal states, have garnered significant interest for their potential to simulate exotic quantum phases [60,61] and for applications in quantum information processing [106].

In systems with full SU(3) symmetry, both the kinetic energy and interactions are invariant under global transformations belonging to the SU(3) group. This symmetry arises naturally in ultracold gases of alkaline-earth-like atoms, such as ^{173}Yb or ^{87}Sr, where the nuclear spin degrees of freedom are decoupled from the electronic states due to the zero electronic angular momentum in the ground state. Consequently, atoms can occupy multiple hyperfine states that interact identically, realizing an SU(N) symmetry with N up to the number of accessible hyperfine states.

In this article, we are particularly interested in 1D interacting Fermi systems and on the effects of spin–orbit coupling and Rabi fields. For fermions with three internal states, we introduce spin–orbit coupling and Rabi fields similarly to the spin-1 case discussed in Section 2. However, we use the terminology of color-orbit coupling to describe how the center of mass momentum couples with internal states (colors). Thus, we call the internal states Red, Green and Blue (R,G,B) as in SU(3) quark systems, and write a general momentum-space Hamiltonian matrix as

$$\hat{H}_{\rm KS}(k)=\begin{pmatrix}\varepsilon_R(k) & \Omega_{RG} & \Omega_{RB}\\ \Omega^*_{RG} & \varepsilon_G(k) & \Omega_{GB}\\ \Omega^*_{RB} & \Omega^*_{GB} & \varepsilon_B(k)\end{pmatrix}, \tag{52}$$

where $\varepsilon_c(k)=(k-k_c)^2/2m+\eta_c$, with color $c=\{R,G,B\}$. This is a particular example of the 3D case discussed in the literature [60,61]. Considering the experimentally realizable Hamiltonian described in Equation (12) of Section 2, we simplify the general Hamiltonian in Equation (52) by letting $\Omega_{RB}=0$, $\Omega_{RG}=\Omega^*_{RG}=\Omega_{GB}=\Omega^*_{GB}=\Omega$, $k_R=k_T$, $k_G=0$, $k_B=-k_T$, and we set the reference

energies η_c to $\eta_R = -\delta$, $\eta_G = \eta$, $\eta_B = \delta$. This choice sets the independent-particle Hamiltonian matrix to

$$\hat{H}_{\rm KS}(k) = \begin{pmatrix} \varepsilon_R(k) & \Omega & 0 \\ \Omega & \varepsilon_G(k) & \Omega \\ 0 & \Omega & \varepsilon_B(k) \end{pmatrix}, \tag{53}$$

where $\varepsilon_R = (k - k_T)^2/2m - \delta$, $\varepsilon_G = k^2/2m + \eta$, $\varepsilon_B = (k + k_T)^2/2m + \delta$ are the dispersions of the Red, Green and Blue states. Here, k_T is the momentum transfer, and $E_T = k_T^2/2m$ is the associated transfer energy. The notation used here is similar to that described in the spin-1 matrix of Equation (12) and in the illustration shown in Figure 1(b): Ω describes a Rabi coupling, δ represents the detuning, and η is a reference energy. In our 1D analysis, we converted the 3D notation used in Equation (12) via the following mapping: $k_x \to k$, $\mathbf{k}_\perp \to \mathbf{0}$, and $k_T \to k_T$ for momenta, as well as $\delta \to \delta$, $\eta \to \eta$ and $\Omega_R/2 \to \Omega$ for energies.

Using a compact notation, we rewrite

$$\hat{H}_{\rm KS}(k) = \varepsilon(k) I - h_x J_x - h_z J_z + b_z J_z^2, \tag{54}$$

where I is the identity matrix and J_ℓ are spin-1 angular momentum matrices

$$J_x = \frac{1}{\sqrt{2}} \begin{pmatrix} 0 & 1 & 0 \\ 1 & 0 & 1 \\ 0 & 1 & 0 \end{pmatrix}, \quad J_y = \frac{1}{\sqrt{2}\mathrm{i}} \begin{pmatrix} 0 & 1 & 0 \\ -1 & 0 & 1 \\ 0 & -1 & 0 \end{pmatrix}, \quad J_z = \begin{pmatrix} 1 & 0 & 0 \\ 0 & 0 & 0 \\ 0 & 0 & -1 \end{pmatrix}.$$

The coefficients that multiply the matrices are $\varepsilon(k) = k^2/2m + \eta$ corresponding to a shifted kinetic energy, $h_x = -\sqrt{2}\Omega$ describing a color-flip (Rabi) field, $h_z(k) = 2kk_T/2m + \delta$ reflecting the color-orbit coupling, and $b_z = k_T^2/2m - \eta$ representing the quadrupolar field. Notice that the quadrupolar term $b_z J_z^2$ lies beyond the realm of the angular momentum SO(3) Lie Group for the spin-1 representation (the 3-representation of SU(2), also called the ajoint representation), requiring the larger SU(3) Lie Group to cover the Hilbert space of the Hamiltonian. As discussed later, we do not use directly the eight Gell-Mann matrices to cover SU(3), but rather use three angular momentum matrices J_ℓ and five quadrupolar tensor matrices $J_\ell J_{\ell'}$ (from the set of nine) to cover the SU(3) space, where $\{\ell, \ell'\} \in \{x, y, z\}$.

We write the independent particle Hamiltonian in second-quantized notation as

$$\hat{H}_{\rm kin} = \sum_k \mathbf{F}^\dagger(k) \hat{H}_{\rm KS}(k) \mathbf{F}(k), \tag{55}$$

where the spinor operator $\mathbf{F}^\dagger(k) = \left(f_R^\dagger(k) \; f_G^\dagger(k) \; f_B^\dagger(k) \right)$ creates fermions with colors $\{R, G, B\}$ and momentum k. The SU(3)-invariant interaction Hamiltonian has the structure

$$\hat{H}_{\rm int} = V_0 \sum_{c \neq c'} \int_0^{L_b} \mathrm{d}x' \int_0^{L_b} \mathrm{d}x \hat{n}_c(x) \hat{n}_{c'}(x') g(|x - x'|), \tag{56}$$

where L_b is the length of system, $\hat{n}_c(x) = \psi_c^\dagger(x)\psi_c(x)$ is the local color density operator with color label $c = \{R, G, B\}$, V_0 is the interaction strength with dimensions of energy, and $g(|x - x'|)$ is a dimensionless function that controls the interaction range R_0.

As we shall see next, color-orbit coupling and color-flip fields change dramatically the eigenvalues and eigenstates of the Hamiltonian in Equation (55).

5.1. *Color-orbit-mixed energy dispersions*

The independent-particle Hamiltonian in Equation (55) is diagonalized via a change of basis implemented by a unitary matrix $R(k)$ satisfying $R(k)R^\dagger(k) = I$. Defining the new basis state by the labels $\{\Uparrow, 0, \Downarrow\}$, then the new creation operators are

$$\mathbf{\Phi}^\dagger(k) = \left(\phi_\Uparrow^\dagger(k) \; \phi_0^\dagger(k) \; \phi_\Downarrow^\dagger(k) \right) = \left(f_R^\dagger(k) \; f_G^\dagger(k) \; f_B^\dagger(k) \right) R^\dagger(k),$$

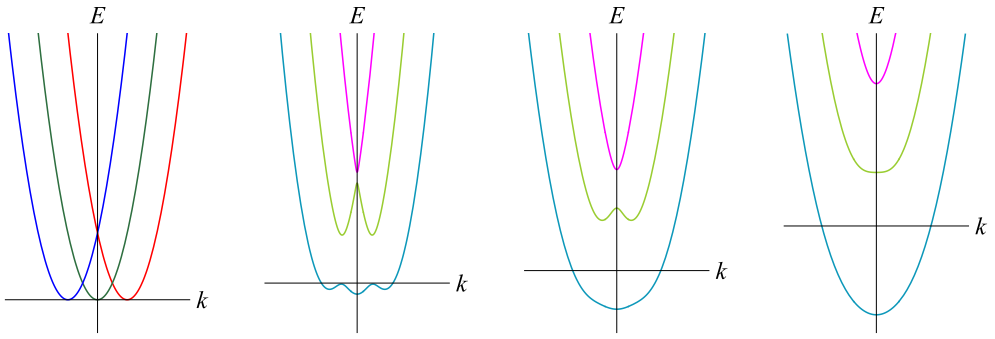

(a) $h_x/E_T = 0$ **(b)** $h_x/E_T = 0.35$ **(c)** $h_x/E_T = 1$ **(d)** $h_x/E_T = 2.1$

Figure 6. Schematic plots of the dispersion relations $\mathscr{E}_\alpha(k)$, with $\alpha \in \{\Uparrow, 0, \Downarrow\}$, for various h_x/E_T, where $E_T = k_T^2/2m$. The unit of momentum is k_T and the unit of energy is E_T. The values of h_x/E_T are indicated in each panel. In (a), the eigenmodes are the same as the internal states $\{R, G, B\}$, and are color-coded as red, green and blue solid lines correspondingly. In (b), (c) and (d), the eigenmodes are labeled by $\{\Uparrow, 0, \Downarrow\}$, and are color-coded as blue-green, yellow-green, and magenta solid lines respectively.

where $R(k)$ written in matrix form is

$$R(k) = \begin{pmatrix} R_{\Uparrow R}(k) & R_{\Uparrow G}(k) & R_{\Uparrow B}(k) \\ R_{0R}(k) & R_{0G}(k) & R_{0B}(k) \\ R_{\Downarrow R}(k) & R_{\Downarrow G}(k) & R_{\Downarrow B}(k) \end{pmatrix}. \tag{57}$$

Due to the presence of the quadratic term $b_z J_z^2$ in the Hamiltonian, $R(k)$ is a general SU(3) matrix and cannot be expressed as a linear combinations of angular momentum operators. The diagonalized independent-particle Hamiltonian matrix is

$$\hat{H}_{\rm MC}(k) = R(k)\hat{H}_{\rm KS}(k)R^\dagger(k) = \begin{pmatrix} \mathscr{E}_\Uparrow(k) & 0 & 0 \\ 0 & \mathscr{E}_0(k) & 0 \\ 0 & 0 & \mathscr{E}_\Downarrow(k) \end{pmatrix}, \tag{58}$$

where $\mathscr{E}_\alpha(k)$ are the eigenenergies with $\alpha \in \{\Uparrow, 0, \Downarrow\}$. These results are analogous to the 3D case [60,61]. In the mixed-color basis, the second-quantized kinetic energy Hamiltonian becomes

$$\hat{H}_{\rm kin} = \sum_k \mathbf{\Phi}^\dagger(k)\hat{H}_{\rm MC}(k)\mathbf{\Phi}(k) = \sum_k \mathscr{E}_\alpha(k)\phi_\alpha^\dagger(k)\phi_\alpha(k). \tag{59}$$

In Figure 6, we show schematically the eigenvalues (dispersion relations) $\mathscr{E}_\alpha(k)$, using $E_T = k_T^2/2m$ as the unit of energy and k_T as the unit of momentum, for various h_x/E_T. There are four qualitative different cases illustrated in panels (a), (b), (c) and (d).

In Figure 6(a), there is no Rabi field $h_x/E_T = 0$, but the momentum transfer is for $+k_T$ for the R band, zero (0) for the G band, and $-k_T$ for the B band. In this case, the system is equivalent to the situation where there is no SOC and the $\{R, G, B\}$ bands are triply degenerate due to a color-gauge symmetry, where the momentum shifts $+k_T$ and $-k_T$ can be gauged away in analogy with the lattice case [107,108].

In Figure 6(b), the dispersions of the $\{\Uparrow, 0, \Downarrow\}$ bands are shown for $h_x/E_T = 0.35$, where the Rabi field is relatively weak in comparison to E_T. In this case, the lowest band ($\Uparrow$) has triple minima and double maxima (blue-green solid line), the middle band (0) has double minima and single maximum (yellow-green solid line), and the highest band ($\Downarrow$) has a single minimum (magenta solid line). For the lowest band ($\Uparrow$), the energy at $k = 0$ is always lower than the local energy minima at $k = \pm k_{\rm min}$, provided that $|h_x|/E_T < 0.544$.

In Figure 6(c), the color-flip (Rabi) field h_x is comparable to the momentum transfer energy E_T, that is, $h_x/E_T = 1$, such that the lowest band ($\Uparrow$) has a single minimum, the middle band (0) has double minima and a single maximum, while the highest band ($\Downarrow$) has a single minimum. This behavior occurs in the range $0.544 < |h_x|/E_T < 2.000$.

In Figure 6(d), the color-flip (Rabi) field h_x is sufficiently strong in comparison to E_T, that is, $|h_x|/E_T > 2.000$, such that all three bands $\{\Uparrow, 0, \Downarrow\}$ have single minima.

In summary, when the color-flip (Rabi) field h_x is zero, the system has spin-gauge symmetry and is equivalent to the situation without SOC. However, when the color-flip field h_x exists there are qualitative changes in the eigenenergies. The highest band ($\Downarrow$) has always a single minimum as shown in panels (b), (c) and (d) of Figure 6. The middle band (0) has double minima and a single maximum when $|h_x|/E_T < 2.000$, as shown in panels (b) and (c) of Figure 6, and has a single minimum when $|h_x|/E_T > 2.000$, as shown in panel (d) of Figure 6. The lowest band ($\Uparrow$) has triple minima and double maxima when $|h_x|/E_T < 0.544$, as illustrated in panel (b) of Figure 6, and has a single minimum when $|h_x|/E_T > 0.544$, as seen in panels (c) and (d) of Figure 6. Now that we have identified the regimes where the eigenvalues $\mathscr{E}_{\Uparrow}(k)$, $\mathscr{E}_0(k)$ and $\mathscr{E}_{\Downarrow}(k)$ change qualitatively, we discuss next the phase diagram and the velocities of the collective (boson) modes.

5.2. *Phase diagram and velocities of boson modes*

In our analysis of the phase diagram for SU(3) fermions, we use $E_T = k_T^2/2m$ and k_T as our energy and momentum scales, respectively, and discuss initially the case of no interactions. For our Fermi system with three internal states, the phase diagram of chemical potential μ/E_T versus Rabi field h_x/E_T is obtained by monitoring the topology of the Fermi surfaces associated with the energy eigenvalues $\mathscr{E}_{\Uparrow}(k)$, $\mathscr{E}_0(k)$ and $\mathscr{E}_{\Downarrow}(k)$. Similarly to the SU(2) case, as the chemical potential varies, the change in the number of Fermi points N_F determines the number of collective modes $N_C = N_F/2$ and defines topological quantum phase transitions of the Lifshitz-type [93–95].

In Figure 7(a), we show the phase diagram of μ/E_T versus h_x/E_T, which is obtained similarly to the SU(2) case, that is, by tracking the topology of the Fermi surfaces and the number of Fermi points N_F. The black solid lines separate phases where the number of collective modes $N_C = N_F/2$ is different, the gray dashed lines describe the locations where the number of minima for the two lowest-energy bands changes, as seen in Figure 6, and the red solid line represents a fixed density curve for $n = 1.2k_T$, where n is the total density in 1D. Long-wavelength and low-energy properties of the collective modes arise from the linearization around the Fermi points and the bosonization process discussed next.

When three degenerate bands are involved, that is, in the absence of color-orbit coupling and color-flip (Rabi) fields where SU(3) is fully preserved, it is natural to seek for analogous effects to spin–charge separation found in SU(2) invariant Tomonaga–Luttinger liquids. Furthermore, when SU(3) symmetry is explicitly broken, due to color-orbit coupling and color-flip fields (see Figure 6), the Fermi system becomes a non-degenerate three-, two- or one-band Tomonaga–Luttinger liquid, depending on the location of the chemical potential. The properties of this three-band Fermi system is explored via a generalized bosonization technique that allows for an analysis of its collective modes. Similar to the standard bosonization technique [4,5], as well as the SU(2) case discussed in Section 4.1 and found in the literature [90], we linearize $\hat{H}_{\rm kin}$ in Equation (59) around the chemical potential giving

$$\hat{H}_{\rm kin} = \sum_{k\alpha r} \{\mu + {\rm sgn}(r)\, v_\alpha [k - {\rm sgn}(r)\, k_{\mu\alpha}]\} \phi^\dagger_{\alpha r}(k) \phi_{\alpha r}(k). \tag{60}$$

Here, $r \in \{L, R\}$ represents left-going or right-going fermions with ${\rm sgn}(L) = -1$ and ${\rm sgn}(R) = 1$, v_α is the velocity at the positive momenta $k_{\mu\alpha}$ where the chemical potential μ intersects band α, that is, $v_{\mu\alpha} = {\rm d}\mathscr{E}_\alpha(k)/{\rm d}k$, and the operator $\phi^\dagger_{\alpha r}(k)$ creates a fermion with momentum k in

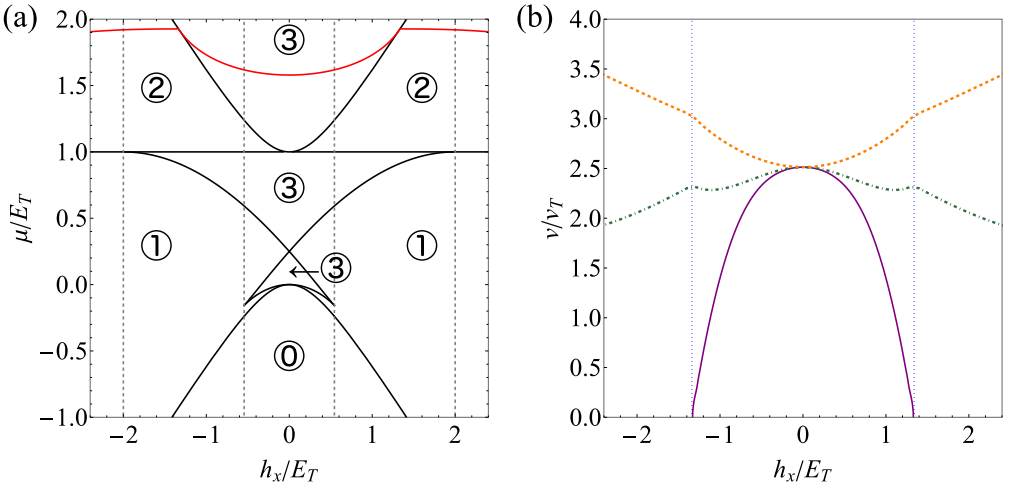

Figure 7. Phase diagram and velocities of collective modes. In panel (a), we show the phase diagram in the plane of μ/E_T versus h_x/E_T. The black solid lines separate phases with different number of collective modes N_C. The values of N_C are indicated by the circled numbers. The gray dashed lines show the location where the number of minima of the two lowest-energy bands changes: the lines at $|h_x|/E_T = \pm 2.000$ separate double minima and single maximum ($|h_x|/E_T < 2.000$) from a single minimum ($|h_x|/E_T < 2.000$) for the middle band (0), and the lines at $|h_x|/E_T = \pm 0.544$ separate triple minima and double maxima ($|h_x|/E_T < 0.544$) from a single minimum ($|h_x|/E_T > 0.544$) for the lowest band ($\Uparrow$). The red solid line represents a constant density curve with $n = 1.2k_T$, where n is the total density in 1D. In panel (b), we show the collective mode velocities $v_\Uparrow$, v_0 and $v_\Downarrow$ along the red curve, shown in panel (a), for non-interacting fermions with energy bands labeled by $\{\Uparrow, 0, \Downarrow\}$. The orange dashed line indicates $v_\Uparrow$, the green dot-dashed line describes v_0, and the purple solid line represents $v_\Downarrow$. In panel (b), the blue dotted lines show the locations where the red solid and the black solid lines intersect in panel (a), revealing a phase change. The number of collective modes changes from $N_C = 2$ to $N_C = 3$ at $h_x/E_T = -1.340$ and from from $N_C = 3$ to $N_C = 2$ at $h_x/E_T = +1.340$.

band α and branch r. Both v_α and $k_{\mu\alpha}$ depend on k_T, h_x and μ. The reference Hamiltonian $\hat{H}_0 = \sum_{k\alpha r} \mu \phi^\dagger_{\alpha r}(k)\phi_{\alpha r}(k)$, corresponding to the energy $E_0 = N\mu$, where N is the total number of fermions, is set to zero without loss of generality. Thus, like in the SU(2) case, we drop this reference term from the kinetic energy operator $\hat{H}_{\rm kin}$ from now on.

To bosonize $\hat{H}_{\rm kin}$, we first define the standard density operator in the momentum space

$$\hat{\rho}_{\alpha r}(q) = \sum_k \phi^\dagger_{\alpha r}(k)\phi_{\alpha r}(k+q), \tag{61}$$

where $\alpha \in \{\Uparrow, 0, \Downarrow\}$ and use the commutation relation

$$[\hat{H}_{\rm kin}, \hat{\rho}_{\alpha r}(q)] = -{\rm sgn}(r)\, v_\alpha q \hat{\rho}_{\alpha r}(q). \tag{62}$$

Combining the last two expressions gives

$$\hat{H}_{\rm kin} = \frac{2\pi}{L_b} \sum_{q>0,\alpha r} v_\alpha \hat{\rho}_{\alpha r}(-q)\hat{\rho}_{\alpha r}(q) \tag{63}$$

in terms of density operators defined in Equation (61), where L_b is the length of the system. The kinetic energy operator is bosonized via the relation

$$b^\dagger_\alpha(q) = \sqrt{\frac{2\pi}{|q|L_b}} \sum_r \Theta\big(-\mathrm{sgn}(r)q\big)\hat{\rho}_{\alpha r}(q), \tag{64}$$

where $\Theta(z)$ is the Heaviside step function, leading to

$$\hat{H}_{\rm kin} = \sum_{q\alpha} v_\alpha |q| b^\dagger_\alpha(q) b_\alpha(q) + K_\Omega, \tag{65}$$

where v_α represents the velocity of the collective mode, labeled by the band index α, in the absence of interactions, and $K_\Omega = \sum_{q>0,\alpha} |q v_\alpha|$. As expected, without interactions, the collective mode velocities are just the Fermi velocities v_α at $k = k_{\mu\alpha}$, but they are functions of the color-flip (Rabi) fields h_x, color-orbit coupling parameter k_T and chemical potential μ or density n.

In Figure 7(b), we show the velocities of the collective modes as a function of h_x, at a fixed density $n = 1.2k_T$, corresponding to the red solid curve in Figure 7(a). The orange dashed line, the green dot-dashed line and the purple solid line indicate the collective mode velocities $v_{\Uparrow}$, v_0, and $v_{\Downarrow}$, respectively. The blue dotted lines show that the number of collective modes changes from $N_{\rm C} = 2$ to $N_{\rm C} = 3$ at $h_x/E_T = -1.340$ and from $N_{\rm C} = 3$ to $N_{\rm C} = 2$ at $h_x/E_T = +1.340$.

Having discussed the bosonization procedure for non-interacting SU(3) fermions in the presence of color-orbit coupling and color-flipping (Rabi) fields, it is clear that among the open questions is the effect of SU(3) symmetric interactions in changing the collective mode velocities, spectral weight and internal properties (quantum numbers), as discussed next.

5.3. *Open questions for SU(3) fermions*

Without SU(3) symmetric interactions, the emergent boson modes $b^\dagger_\alpha(q)$ and $b_\alpha(q)$ are simply related to the density operators $\hat{\rho}^\dagger_{\alpha r}(q)$ and $\hat{\rho}_{\alpha r}(q)$, as seen in Equation (64). However, SU(3) symmetric interactions $\hat{H}_{\rm int}$, given in Equation (56), are expected to introduce additional bilinears involving $\hat{\rho}^\dagger_{\alpha r}(q)$ and $\hat{\rho}_{\alpha r}(q)$ that require a generalized Bogoliubov transformation to diagonalize the total Hamiltonian $\hat{H} = \hat{H}_{\rm kin} + \hat{H}_{\rm int}$. In analogy to the SU(2) case, we identify the eigenmodes of $\hat{H}$ with the final bosonic operators $d^\dagger_\ell(q)$ and $d_\ell(q)$, but now ℓ can have a maximum of three flavors, that is, $\ell = \{1,2,3\}$.

As discussed in Section 4.2, for fermions with two internal states, the boson operators $d^\dagger_\ell(q)$ and $d_\ell(q)$ covered the SU(2) space and were decomposed into charge (scalar) and spin (vector) sectors. When Rabi fields and SOC are zero, the degenerate Fermi bands and the SU(2) invariant interaction lead to the standard spin–charge separation, and when Rabi field and SOC are nonzero, the bosonic modes become Weyl bosons, with a helical structure expressed in terms of a mixture of charge- and spin-density operators. The coverage of the SU(2) Lie group leads to a singlet sector that transforms like the identity (charge density), and a triplet sector that transforms like angular momentum (spin density).

In the SU(3) case, it is natural to conjecture that the final bosonic operators $d^\dagger_\ell(q)$ and $d_\ell(q)$ are decomposed into singlet (charge density), triplet (spin density) and quintet (quadrupolar density) sectors. Hence, the set of operators $\{\hat{\rho}, \hat{\mathbf{J}}, \hat{\mathbf{K}}\}$, where $\hat{\rho}$ is the density, $\hat{\mathbf{J}}$ is the angular momentum, and $\hat{\mathbf{K}}$ is the symmetric quadrupolar tensor quintet

$$\hat{\mathbf{K}} = \big(\tfrac{1}{2}\{\hat{J}_x, \hat{J}_y\}, \tfrac{1}{2}\{\hat{J}_y, \hat{J}_z\}, \tfrac{1}{2}\{\hat{J}_z, \hat{J}_x\}, \hat{J}_x^2 - \tfrac{1}{3}\hat{\rho}, \hat{J}_y^2 - \tfrac{1}{3}\hat{\rho}\big)^T, \tag{66}$$

provide a physically transparent coverage of SU(3), which is preferable, instead of using the Gell-Mann matrices used for quark SU(3) physics. Here, $\{\hat{A}, \hat{B}\}$ represents the anti-commutator of operators $\hat{A}$ and $\hat{B}$. Hence, the final boson operators may be decomposed as

$$d^\dagger_\ell(q) = \sum_r \big[A_{\ell r}(q)\hat{\rho}_r(q) + \mathbf{B}_{\ell r}(q)\cdot\hat{\mathbf{J}}_r(q) + \mathbf{C}_{\ell r}(q)\cdot\hat{\mathbf{K}}_r(q)\big], \tag{67}$$

where $\hat{\rho}(q)$, $\hat{\mathbf{J}}(q)$, and $\hat{\mathbf{K}}(q)$ are second-quantized momentum-space fermionic representations of $\{\hat{\rho}, \hat{\mathbf{J}}, \hat{\mathbf{K}}\}$, respectively, and the label r represents either left (L) or right (R) going fermions.

If the conjectured decomposition above holds for bosonic eigenmodes of SU(3) Fermi systems, several open questions arise both with and without color-orbit coupling and color-flip (Rabi) fields: If no color-orbit or color-flip fields are present, is there spin–charge–quadrupole separation when interactions are included? Is there an expanded analogy to spin–charge separation found for SU(2)? Are there separated charge, spin and quadrupolar density modes? Furthermore, if color-orbit coupling, color-flip fields, and interactions are present, what are the extensions of Weyl bosons to the SU(3) case? Do helical or nematic modes arise due to the spin or quadrupolar sectors?

Since there the quadrupolar operator has a tensorial structure, what experimentally measurable response functions can reveal this feature? Is there an extension of the dynamical structure factor tensor $S_{ij}(q,\omega)$, found for SU(2) systems, that can be measured for the SU(3) case? Selection rules involving quadrupolar operators are different from those involving angular momentum operators: can they be used to detect the tensorial nature of the bosonic modes?[2]

Given the expected tensorial, vector and scalar components of the SU(3) bosonic modes $d_\ell(q)$ is there a closer connection to spin-squeezing [109], magnetization [110], and topology [111] of condensed spin-1 bosons?

Experimental studies of SU(3) fermions with color-orbit and color-flip (Rabi) fields remain challenging. However, recent advances have realized SU(3) color-orbit coupling in a laser-trapped ultracold gas of ^{87}Sr [112]. Moreover, the development of box potentials offers promising prospects for trapping fermions with three internal states [97]. These developments suggest that similar investigations using other atomic species, such as ^{173}Yb, may become feasible in the near future.

Having discussed several open questions for SU(3) fermions in the presence or absence of color-orbit coupling and color-flip (Rabi) fields, we present, next, our conclusions and general outlook.

6. Conclusions and general outlook

We have discussed the current research status and open questions regarding the effects of spin–orbit coupling and Rabi fields for SU(2) Tomonaga–Luttinger liquids and color-orbit coupling and color-flip fields for SU(3) Tomonaga–Luttinger liquids. In this article, we focused on one dimensional systems realized in ultracold fermions, but some of the current status results and open questions when spin–orbit (color-orbit) and Rabi (color-flip) fields are present are also applicable to standard condensed matter and to two-dimensional and three-dimensional systems. We concentrated on one-dimensional systems, because several intermediate and advanced analytical results can be obtained using the bosonization method.

For SU(2) systems, the emergence of Weyl bosons, that is, helical, massless pseudo-spin 1/2 bosons, is not a phenomenon only restricted to one dimension, but also arises in two and three dimensions. The helicity induced by the spin–orbit and Rabi fields created by Raman processes and affecting fermionic states is transferred to the charge and spin density sectors creating helical collective excitations. The analysis in one dimension is more beautiful, because we can start from charge and spin separated systems, and create Weyl bosons by coupling these two channels via spin–orbit and Rabi fields. However, we expect that in two and three dimensions, where charge and spin densities are not separated, Weyl bosons will also emerge due to spin–orbit coupling and

[2] This question was inspired by a related question that Wolfgang Ketterle asked, regarding C. A. R. Sá de Melo's presentation at the Institut Henri Poincaré, covering the atomic processes and the selection rules that are needed to detect experimentally SU(3) tensorial modes.

Rabi fields and could be detected by measuring the components of the dynamical structure factor tensor, just like in one dimension. Currently, in any dimension, the experimental exploration of this phenomenon for ^{6}Li, ^{40}K, ^{173}Yb and ^{87}Sr is very difficult, because of difficulties associated with specific atomic properties or technicalities that prevent the creation of simultaneous spin–orbit coupling and Rabi fields at sufficiently low temperatures.

For SU(3) systems, the ideal candidates are ^{173}Yb and ^{87}Sr, where the interactions are naturally SU(N) symmetric, with $N \leq 6$ in the former and $N \leq 10$ in the latter. When $N = 3$, both candidates are SU(3) symmetric without color-orbit and color-flip (Rabi) fields. The existence of up to three collective modes with scalar (singlet), vector (triplet) and tensorial (quintuplet) components are expected when expressed in terms of the charge, spin and quadrupolar densities. Thus, the collective bosonic modes are anticipated to be much more exotic that the Weyl bosons found in the SU(2) case. Although one dimensional systems allow for several analytical results and transparent symmetry considerations arising directly from bosonization, similar results are also envisaged in two and three dimensions. However, experimental investigations of color-orbit and color-flip (Rabi) fields of interacting SU(3) fermions, in any dimension, have not yet been performed due to technical difficulties.

Due to the absence of experiments exploring interacting SU(2) or SU(3) fermions in the presence of spin–orbit and Rabi fields or color-orbit and color-flip fields, the entire presentation above is currently only of theoretical interest. However, as an outlook, it is important to emphasize that SU(2) or SU(3) symmetric interactions are not necessary for the emergence of Weyl bosons or tensorial collective bosonic modes in one, two or three dimensions. This means that for any interacting ultracold Fermi system with two or three internal states, it is sufficient to create spin–orbit and Rabi couplings or color-orbit and color-flip couplings to produce the exotic collective modes discussed above. Furthermore, in the context of standard condensed matter systems, it is also sufficient to find a material, with either two or three bands, and essentially any kind of spin–orbit coupling and Zeeman fields to produce similar types of collective modes.

On the one hand, the experimental outlook for ultracold fermions is to find a way to overcome the difficulties in standard systems such as ^{6}Li, ^{40}K, ^{173}Yb and ^{87}Sr or to explore novel systems such as ^{171}Dy or ^{173}Dy; on the other hand, the experimental outlook for standard condensed matter, is to find solid state materials that meet the appropriate theoretical requirements. In the mean time, while we await experimental progress, there are plenty of open theoretical questions that need to be addressed.

Declaration of interests

The authors do not work for, advise, own shares in, or receive funds from any organization that could benefit from this article, and have declared no affiliations other than their research organizations.

Acknowledgements

CARSM would like to acknowledge the Institut Henri Poincaré for its hospitality, the Mercator Fellowship from the German Research Foundation (DFG) for support, and Yvan Castin, Wolfgang Ketterle, and Thierry Giamarchi for discussions.

References

[1] S.-I. Tomonaga, "Remarks on Bloch's method of sound waves applied to many-fermion problems", *Prog. Theor. Phys.* **5** (1950), no. 4, pp. 544–569.

[2] J. M. Luttinger, "An exactly soluble model of a manyfermion system", *J. Math. Phys.* **4** (1963), no. 9, pp. 1154–1162.

[3] F. D. M. Haldane, "'Luttinger liquid theory' of one-dimensional quantum fluids. I. Properties of the Luttinger model and their extension to the general 1D interacting spinless Fermi gas", *J. Phys. C: Solid State Phys.* **14** (1981), no. 19, pp. 2585–2609.

[4] T. Giamarchi, *Quantum Physics in One Dimension*, Oxford University Press: Oxford, 2003.

[5] A. Altland and B. Simons, *Condensed Matter Field Theory*, 3rd edition, Cambridge University Press: Cambridge, 2023.

[6] A. Imambekov, T. L. Schmidt and L. I. Glazman, "One-dimensional quantum liquids: beyond the Luttinger liquid paradigm", *Rev. Mod. Phys.* **84** (2012), pp. 1253–1306.

[7] A. J. Niemi and N. R. Walet, "Splitting the gluon?", *Phys. Rev. D* **72** (2005), article no. 054007.

[8] L. Faddeev and A. J. Niemi, "Spin-charge separation, conformal covariance and the SU(2) Yang–Mills theory", *Nucl. Phys. B* **776** (2007), no. 1, pp. 38–65.

[9] M. N. Chernodub and A. J. Niemi, "Spin-charge separation and the Pauli electron", *JETP Lett.* **85** (2007), no. 8, pp. 353–357.

[10] G. A. Diamandis, B. C. Georgalas and N. E. Mavromatos, "N=1 supersymmetric spin-charge separation in effective gauge theories of planar magnetic superconductors", *Mod. Phys. Lett. A* **13** (1998), no. 05, pp. 387–404.

[11] C. Xiong, "From the fourth color to spin-charge separation: Neutrinos and spinons", *Mod. Phys. Lett. A* **30** (2015), no. 25, article no. 1530021.

[12] C. Kim, A. Y. Matsuura, Z.-X. Shen, N. Motoyama, H. Eisaki, S. Uchida, T. Tohyama and S. Maekawa, "Observation of spin-charge separation in one-dimensional $SrCuO_2$", *Phys. Rev. Lett.* **77** (1996), pp. 4054–4057.

[13] B. J. Kim et al., "Distinct spinon and holon dispersions in photoemission spectral functions from one-dimensional SrCuO2", *Nat. Phys.* **2** (2006), no. 6, pp. 397–401.

[14] O. M. Auslaender, A. Yacoby, R. de Picciotto, K. W. Baldwin, L. N. Pfeiffer and K. W. West, "Tunneling spectroscopy of the elementary excitations in a one-dimensional wire", *Science* **295** (2002), no. 5556, pp. 825–828.

[15] O. M. Auslaender, H. Steinberg, A. Yacoby, Y. Tserkovnyak, B. I. Halperin, K. W. Baldwin, L. N. Pfeiffer and K. W. West, "Spin-charge separation and localization in one dimension", *Science* **308** (2005), no. 5718, pp. 88–92.

[16] R. Senaratne et al., "Spin-charge separation in a one-dimensional Fermi gas with tunable interactions", *Science* **376** (2022), no. 6599, pp. 1305–1308.

[17] D. Cavazos-Cavazos, R. Senaratne, A. Kafle and R. G. Hulet, "Thermal disruption of a Luttinger liquid", *Nat. Commun.* **14** (2023), no. 1, article no. 3154.

[18] J. Sinova, S. O. Valenzuela, J. Wunderlich, C. H. Back and T. Jungwirth, "Spin Hall effects", *Rev. Mod. Phys.* **87** (2015), pp. 1213–1260.

[19] T. Kawada, M. Kawaguchi, T. Funato, H. Kohno and M. Hayashi, "Acoustic spin Hall effect in strong spin–orbit metals", *Sci. Adv.* **7** (2021), no. 2, article no. eabd9697.

[20] M. Z. Hasan and C. L. Kane, "Colloquium: topological insulators", *Rev. Mod. Phys.* **82** (2010), pp. 3045–3067.

[21] X.-L. Qi and S.-C. Zhang, "Topological insulators and superconductors", *Rev. Mod. Phys.* **83** (2011), pp. 1057–1110.

[22] M. Sato and Y. Ando, "Topological superconductors: a review", *Rep. Prog. Phys.* **80** (2017), no. 7, article no. 076501.

[23] H. D. Scammell, J. Ingham, M. Geier and T. Li, "Intrinsic first- and higher-order topological superconductivity in a doped topological insulator", *Phys. Rev. B* **105** (2022), article no. 195149.

[24] M. Zeng, D.-H. Xu, Z.-M. Wang and L.-H. Hu, "Spin-orbit coupled superconductivity with spin-singlet nonunitary pairing", *Phys. Rev. B* **107** (2023), article no. 094507.

[25] E. Rashba and V. Sheka, "Combined resonance in electron InSb", *Sov. Phys., Solid State* **3** (1961), no. 6, pp. 1357–1362.

[26] G. Dresselhaus, "Spin-orbit coupling effects in zinc blende structures", *Phys. Rev.* **100** (1955), pp. 580–586.

[27] Y. A. Bychkov and É. I. Rashba, "Properties of a 2D electron gas with lifted spectral degeneracy", *JETP Lett.* **39** (1984), no. 2, pp. 78–81.

[28] J. Sinova and A. H. MacDonald, "Theory of spin–orbit effects in semiconductors", *Semicond. Semimetals* **82** (2008), pp. 45–87.

[29] S. Schott et al., "Tuning the effective spin–orbit coupling in molecular semiconductors", *Nat. Commun.* **8** (2017), no. 1, article no. 15200.

[30] J. Chen, K. Wu, W. Hu and J. Yang, "Spin–orbit coupling in 2D semiconductors: a theoretical perspective", *J. Phys. Chem. Lett.* **12** (2021), no. 51, pp. 12256–12268.

[31] E. Marcellina, A. R. Hamilton, R. Winkler and D. Culcer, "Spin-orbit interactions in inversion-asymmetric two-dimensional hole systems: a variational analysis", *Phys. Rev. B* **95** (2017), article no. 075305.

[32] D. Shcherbakov et al., "Layer- and gate-tunable spin–orbit coupling in a high-mobility few-layer semiconductor", *Sci. Adv.* **7** (2021), no. 5, article no. eabe2892.

[33] D. L. Campbell, G. Juzeliūnas and I. B. Spielman, "Realistic Rashba and Dresselhaus spin–orbit coupling for neutral atoms", *Phys. Rev. A* **84** (2011), article no. 025602.
[34] V. Galitski and I. B. Spielman, "Spin–orbit coupling in quantum gases", *Nature* **494** (2013), no. 7435, pp. 49–54.
[35] Y.-J. Lin, K. Jiménez-García and I. B. Spielman, "Spin–orbit-coupled Bose–Einstein condensates", *Nature* **471** (2011), no. 7336, pp. 83–86.
[36] M. Atala, M. Aidelsburger, M. Lohse, J. T. Barreiro, B. Paredes and I. Bloch, "Observation of chiral currents with ultracold atoms in bosonic ladders", *Nat. Phys.* **10** (2014), no. 8, pp. 588–593.
[37] A. Frölian, C. S. Chisholm, E. Neri, C. R. Cabrera, R. Ramos, A. Celi and L. Tarruell, "Realizing a 1D topological gauge theory in an optically dressed BEC", *Nature* **608** (2022), no. 7922, pp. 293–297.
[38] L. W. Cheuk, A. T. Sommer, Z. Hadzibabic, T. Yefsah, W. S. Bakr and M. W. Zwierlein, "Spin-injection spectroscopy of a spin-orbit coupled Fermi gas", *Phys. Rev. Lett.* **109** (2012), article no. 095302.
[39] M. Mancini et al., "Observation of chiral edge states with neutral fermions in synthetic Hall ribbons", *Science* **349** (2015), no. 6255, pp. 1510–1513.
[40] S. Kolkowitz et al., "Spin–orbit-coupled fermions in an optical lattice clock", *Nature* **542** (2017), no. 7639, pp. 66–70.
[41] D. L. Campbell and I. B. Spielman, "Rashba realization: Raman with RF", *New J. Phys.* **18** (2016), no. 3, article no. 033035.
[42] L. Huang et al., "Experimental realization of two-dimensional synthetic spin–orbit coupling in ultracold Fermi gases", *Nat. Phys.* **12** (2016), no. 6, pp. 540–544.
[43] A. Valdés-Curiel, D. Trypogeorgos, Q.-Y. Liang, R. P. Anderson and I. B. Spielman, "Topological features without a lattice in Rashba spin–orbit coupled atoms", *Nat. Commun.* **12** (2021), no. 1, article no. 593.
[44] K. Seo, L. Han and C. A. R. Sá de Melo, "Topological phase transitions in ultracold Fermi superfluids: the evolution from Bardeen-Cooper-Schrieffer to Bose-Einstein-condensate superfluids under artificial spin–orbit fields", *Phys. Rev. A* **85** (2012), article no. 033601.
[45] W. Pauli, "The connection between spin and statistics", *Phys. Rev.* **58** (1940), pp. 716–722.
[46] M. K. Gaillard, P. D. Grannis and F. J. Sciulli, "The standard model of particle physics", *Rev. Mod. Phys.* **71** (1999), S96–S111.
[47] S. Weinberg, "The making of the standard model", *Eur. Phys. J. C* **34** (2004), no. 1, pp. 5–13.
[48] P. A. M. Dirac, "The quantum theory of the electron", *Proc. R. Soc. Lond. A* **117** (1928), no. 778, pp. 610–624.
[49] E. Majorana, "Teoria simmetrica dell'elettrone e del positrone", *Nuovo Cimento* **14** (1937), no. 4, pp. 171–184.
[50] H. Weyl, "Elektron und gravitation. I", *Z. Phys.* **56** (1929), no. 5, pp. 330–352.
[51] D. Castelvecchi, "Evidence of elusive Majorana particle dies — but computing hope lives on", *Nature* **591** (2021), no. 7850, pp. 354–355.
[52] O. Vafek and A. Vishwanath, "Dirac fermions in solids: from high-T_c cuprates and graphene to topological insulators and weyl semimetals", *Annu. Rev. Condens. Matter Phys.* **5** (2014), pp. 83–112.
[53] M. Horio et al., "Two-dimensional type-II Dirac fermions in layered oxides", *Nat. Commun.* **9** (2018), no. 1, article no. 3252.
[54] Y. Ran, F. Wang, H. Zhai, A. Vishwanath and D.-H. Lee, "Nodal spin density wave and band topology of the FeAs-based materials", *Phys. Rev. B* **79** (2009), article no. 014505.
[55] P. Richard et al., "Observation of Dirac cone electronic dispersion in $BaFe_2As_2$", *Phys. Rev. Lett.* **104** (2010), article no. 137001.
[56] S. Y. Tan et al., "Observation of Dirac cone band dispersions in FeSe thin films by photoemission spectroscopy", *Phys. Rev. B* **93** (2016), article no. 104513.
[57] K. S. Novoselov, A. K. Geim, S. V. Morozov, D. Jiang, M. I. Katsnelson, I. V. Grigorieva, S. V. Dubonos and A. A. Firsov, "Two-dimensional gas of massless Dirac fermions in graphene", *Nature* **438** (2005), no. 7065, pp. 197–200.
[58] S.-Y. Xu et al., "Discovery of a Weyl fermion semimetal and topological Fermi arcs", *Science* **349** (2015), no. 6248, pp. 613–617.
[59] B. Q. Lv et al., "Experimental discovery of weyl semimetal TaAs", *Phys. Rev. X* **5** (2015), article no. 031013.
[60] D. M. Kurkcuoglu and C. A. R. Sá de Melo, "Creating spin-one fermions in the presence of artificial spin–orbit fields: emergent spinor physics and spectroscopic properties", *J. Low-Temp. Phys.* **191** (2018), no. 3, pp. 174–183.
[61] D. M. Kurkcuoglu and C. A. R. Sá de Melo, "Color superfluidity of neutral ultracold fermions in the presence of color-flip and color-orbit fields", *Phys. Rev. A* **97** (2018), article no. 023632.
[62] C. Chin, R. Grimm, P. Julienne and E. Tiesinga, "Feshbach resonances in ultracold gases", *Rev. Mod. Phys.* **82** (2010), pp. 1225–1286.
[63] H. Biss, L. Sobirey, N. Luick, M. Bohlen, J. J. Kinnunen, G. M. Bruun, T. Lompe and H. Moritz, "Excitation spectrum and superfluid gap of an ultracold Fermi gas", *Phys. Rev. Lett.* **128** (2022), article no. 100401.
[64] L. Sobirey, H. Biss, N. Luick, M. Bohlen, H. Moritz and T. Lompe, "Observing the influence of reduced dimensionality on fermionic superfluids", *Phys. Rev. Lett.* **129** (2022), article no. 083601.

[65] M. Chapman and C. A. R. Sá de Melo, "Atoms playing dress-up", *Nature* **471** (2011), no. 7336, pp. 41–42.
[66] P. Wang, Z.-Q. Yu, Z. Fu, J. Miao, L. Huang, S. Chai, H. Zhai and J. Zhang, "Spin-orbit coupled degenerate Fermi gases", *Phys. Rev. Lett.* **109** (2012), article no. 095301.
[67] T. Fukuhara, Y. Takasu, M. Kumakura and Y. Takahashi, "Degenerate Fermi gases of ytterbium", *Phys. Rev. Lett.* **98** (2007), article no. 030401.
[68] Y. Takasu, Y. Fukushima, Y. Nakamura and Y. Takahashi, "Magnetoassociation of a Feshbach molecule and spin–orbit interaction between the ground and electronically excited states", *Phys. Rev. A* **96** (2017), article no. 023602.
[69] B. J. DeSalvo, M. Yan, P. G. Mickelson, Y. N. Martinez de Escobar and T. C. Killian, "Degenerate Fermi gas of ^{87}Sr", *Phys. Rev. Lett.* **105** (2010), article no. 030402.
[70] I. B. Spielman, "Raman processes and effective gauge potentials", *Phys. Rev. A* **79** (2009), article no. 063613.
[71] Y.-J. Lin, R. L. Compton, A. R. Perry, W. D. Phillips, J. V. Porto and I. B. Spielman, "Bose-Einstein condensate in a uniform light-induced vector potential", *Phys. Rev. Lett.* **102** (2009), article no. 130401.
[72] D. C. Mattis and E. H. Lieb, "Exact solution of a manyfermion system and its associated boson field", *J. Math. Phys.* **6** (1965), no. 2, pp. 304–312.
[73] M. Dressel, "Spin-charge separation in quasi one-dimensional organic conductors", *Naturwissenschaften* **90** (2003), no. 8, pp. 337–344.
[74] J. Sólyom, "The Fermi gas model of one-dimensional conductors", *Adv. Phys.* **28** (1979), no. 2, pp. 201–303.
[75] D.-W. Wang, A. J. Millis and S. D. Sarma, "Coulomb Luttinger liquid", *Phys. Rev. B* **64** (2001), no. 19, article no. 193307.
[76] F. He, Y.-Z. Jiang, H.-Q. Lin, R. G. Hulet, H. Pu and X.-W. Guan, "Emergence and disruption of spin-charge separation in one-dimensional repulsive fermions", *Phys. Rev. Lett.* **125** (2020), article no. 190401.
[77] C. N. Yang, "Some exact results for the many-body problem in one dimension with repulsive delta-function interaction", *Phys. Rev. Lett.* **19** (1967), pp. 1312–1315.
[78] M. Gaudin, "Un système à une dimension de fermions en interaction", *Phys. Lett. A* **24** (1967), no. 1, pp. 55–56.
[79] O. Tsyplyatyev, "Splitting of the Fermi point of strongly interacting electrons in one dimension: a nonlinear effect of spin-charge separation", *Phys. Rev. B* **105** (2022), article no. L121112.
[80] P. M. T. Vianez et al., "Observing separate spin and charge Fermi seas in a strongly correlated one-dimensional conductor", *Sci. Adv.* **8** (2022), no. 24, article no. eabm2781.
[81] L. Han and C. A. R. Sá de Melo, "Evolution from BCS to BEC superfluidity in the presence of spin–orbit coupling", *Phys. Rev. A* **85** (2012), article no. 011606.
[82] K. Seo, L. Han and C. A. R. Sá de Melo, "Emergence of Majorana and Dirac particles in ultracold fermions via tunable interactions, spin-orbit effects, and Zeeman fields", *Phys. Rev. Lett.* **109** (2012), article no. 105303.
[83] P. D. Powell, G. Baym and C. A. R. Sá de Melo, "Superfluid transition temperature and fluctuation theory of spin–orbit- and Rabi-coupled fermions with tunable interactions", *Phys. Rev. A* **105** (2022), article no. 063304.
[84] M. Gong, S. Tewari and C. Zhang, "BCS-BEC crossover and topological phase transition in 3D spin-orbit coupled degenerate Fermi gases", *Phys. Rev. Lett.* **107** (2011), article no. 195303.
[85] H. Hu, L. Jiang, X.-J. Liu and H. Pu, "Probing anisotropic superfluidity in atomic Fermi gases with Rashba spin-orbit coupling", *Phys. Rev. Lett.* **107** (2011), article no. 195304.
[86] Z.-Q. Yu and H. Zhai, "Spin-orbit coupled Fermi gases across a Feshbach resonance", *Phys. Rev. Lett.* **107** (2011), article no. 195305.
[87] J. P. A. Devreese, J. Tempere and C. A. R. Sá de Melo, "Effects of spin-orbit coupling on the Berezinskii-Kosterlitz-Thouless transition and the vortex-antivortex structure in two-dimensional Fermi gases", *Phys. Rev. Lett.* **113** (2014), article no. 165304.
[88] J. P. A. Devreese, J. Tempere and C. A. R. Sá de Melo, "Topological phases and collective modes in U(1) and SU(2) sectors of spin–orbit-coupled two-dimensional superfluid Fermi gases", *Phys. Rev. A* **105** (2022), article no. 033304.
[89] R. A. Williams, M. C. Beeler, L. J. LeBlanc, K. Jiménez-García and I. B. Spielman, "Raman-induced interactions in a single-component Fermi gas near an *s*-wave Feshbach resonance", *Phys. Rev. Lett.* **111** (2013), article no. 095301.
[90] X. Zhang and C. A. R. Sá de Melo, "Beyond spin-charge separation: helical modes and topological quantum phase transitions in one-dimensional Fermi gases with spin–orbit and Rabi couplings", preprint, 2024, 2405.20255.
[91] A. Imambekov and L. I. Glazman, "Universal theory of nonlinear Luttinger liquids", *Science* **323** (2009), no. 5911, pp. 228–231.
[92] X. Zhang, *Effects of spin–orbit coupling and Rabi fields in SU(2) and SU(3) symmetric Tomonaga–Luttinger liquids*, PhD thesis, Georgia Institute of Technology, 2025.
[93] I. M. Lifshitz, "Anomalies of electron characteristics of a metal in the high pressure region", *Sov. Phys. JETP* **11** (1960), no. 5, pp. 1130–1135.

[94] R. D. Duncan and C. A. R. Sá de Melo, "Thermodynamic properties in the evolution from BCS to Bose-Einstein condensation for a d-wave superconductor at low temperatures", *Phys. Rev. B* **62** (2000), pp. 9675–9687.
[95] S. S. Botelho and C. A. R. Sá de Melo, "Lifshitz transition in *d*-wave superconductors", *Phys. Rev. B* **71** (2005), article no. 134507.
[96] M. Olshanii, "Atomic scattering in the presence of an external confinement and a gas of impenetrable bosons", *Phys. Rev. Lett.* **81** (1998), pp. 938–941.
[97] N. Navon, R. P. Smith and Z. Hadzibabic, "Quantum gases in optical boxes", *Nat. Phys.* **17** (2021), no. 12, pp. 1334–1341.
[98] K.-N. Schymik, S. Pancaldi, F. Nogrette, D. Barredo, J. Paris, A. Browaeys and T. Lahaye, "Single atoms with 6000-second trapping lifetimes in optical-tweezer arrays at cryogenic temperatures", *Phys. Rev. Appl.* **16** (2021), article no. 034013.
[99] T. F. Schmidutz, I. Gotlibovych, A. L. Gaunt, R. P. Smith, N. Navon and Z. Hadzibabic, "Quantum Joule-Thomson effect in a saturated homogeneous Bose gas", *Phys. Rev. Lett.* **112** (2014), article no. 040403.
[100] G. Källén, "On the definition of the renormalization constants in quantum electrodynamics", *Helv. Phys. Acta* **25** (1952), no. IV, pp. 417–434.
[101] H. Lehmann, "Über Eigenschaften von Ausbreitungsfunktionen und Renormierungskonstanten quantisierter Felder", *Nuovo Cimento* **11** (1954), no. 4, pp. 342–357.
[102] E. H. Moore, "On the reciprocal of the general algebraic matrix", *Bull. Am. Math. Soc.* **26** (1920), pp. 394–395.
[103] R. Penrose, "A generalized inverse for matrices", *Math. Proc. Camb. Philos. Soc.* **51** (1955), no. 3, pp. 406–413.
[104] L. Onsager, "Reciprocal relations in irreversible processes. I", *Phys. Rev.* **37** (1931), pp. 405–426.
[105] L. Onsager, "Reciprocal relations in irreversible processes. II", *Phys. Rev.* **38** (1931), pp. 2265–2279.
[106] F. Scazza, C. Hofrichter, M. Höfer, P. C. De Groot, I. Bloch and S. Fölling, "Observation of two-orbital spin-exchange interactions with ultracold SU(N)-symmetric fermions", *Nat. Phys.* **10** (2014), no. 10, pp. 779–784.
[107] M. H. Yau and C. A. R. Sá de Melo, "SU(3) vs. SU(2) fermions in optical lattices: Color-Hall vs. spin-Hall topological insulators", *EPL* **135** (2021), no. 1, article no. 16001.
[108] M. H. Yau and C. A. R. Sá de Melo, "Eigenspectrum, Chern numbers and phase diagrams of ultracold color-orbit-coupled SU(3) fermions in optical lattices", *Phys. Rev. A* **103** (2021), article no. 043302.
[109] C. D. Hamley, C. S. Gerving, T. M. Hoang, E. M. Bookjans and M. S. Chapman, "Spin-nematic squeezed vacuum in a quantum gas", *Nat. Phys.* **8** (2012), no. 4, pp. 305–308.
[110] H. M. Bharath, M. S. Chapman and C. A. R. Sá de Melo, "Staircase in magnetization and entanglement entropy of spinor condensates", *Phys. Rev. A* **98** (2018), article no. 031601.
[111] B. H. M., M. Boguslawski, M. Barrios, L. Xin and M. S. Chapman, "Exploring non-abelian geometric phases in spin-1 ultracold atoms", *Phys. Rev. Lett.* **123** (2019), article no. 173202.
[112] C. S. Madasu et al., "Experimental realization of a SU(3) color-orbit coupling in an ultracold gas", preprint, 2025, 2502.04714.